

Rubidium 87 D Line Data

Daniel Adam Steck

Oregon Center for Optics and Department of Physics, University of Oregon

Copyright © 2001, by Daniel Adam Steck. All rights reserved.

This material may be distributed only subject to the terms and conditions set forth in the Open Publication License, v1.0 or later (the latest version is presently available at <http://www.opencontent.org/openpub/>). Distribution of substantively modified versions of this document is prohibited without the explicit permission of the copyright holder. Distribution of the work or derivative of the work in any standard (paper) book form is prohibited unless prior permission is obtained from the copyright holder.

Original revision posted 25 September 2001.

This is revision 2.3.3, 28 May 2024.

Cite this document as:

Daniel A. Steck, “Rubidium 87 D Line Data,” available online at <http://steck.us/alkalidata> (revision 2.3.3, 28 May 2024).

Author contact information:

Daniel Steck

Department of Physics

1274 University of Oregon

Eugene, Oregon 97403-1274

dan@steck.us

1 Introduction

In this reference we present many of the physical and optical properties of ^{87}Rb that are relevant to various quantum optics experiments. In particular, we give parameters that are useful in treating the mechanical effects of light on ^{87}Rb atoms. The measured numbers are given with their original references, and the calculated numbers are presented with an overview of their calculation along with references to more comprehensive discussions of their underlying theory. At present, this document is *not* a critical review of experimental data, nor is it even guaranteed to be correct; for any numbers critical to your research, you should consult the original references. We also present a detailed discussion of the calculation of fluorescence scattering rates, because this topic is often not treated clearly in the literature. More details and derivations regarding the theoretical formalism here may be found in Ref. [1].

The current version of this document is available at <http://steck.us/alkalidata>, along with “Cesium D Line Data,” “Sodium D Line Data,” and “Rubidium 85 D Line Data.” This is the *only* permanent URL for this document at present; please do not link to any others. Please send comments, corrections, and suggestions to dan@steck.us.

2 Rubidium 87 Physical and Optical Properties

Some useful fundamental physical constants are given in Table 1. The values given are the 2018 CODATA recommended values, as listed in [2]. Some of the overall physical properties of ^{87}Rb are given in Table 2. Rubidium 87 has 37 electrons, only one of which is in the outermost shell. ^{87}Rb is not a stable isotope of rubidium, decaying to $\beta^- + ^{87}\text{Sr}$ with a total disintegration energy of 0.283 MeV [3] (the only stable isotope is ^{85}Rb), but has an extremely slow decay rate, thus making it effectively stable. This is the only isotope we consider in this reference. The mass is taken from the high-precision measurement of [4], and the density, melting point, boiling point, and heat capacities (for the naturally occurring form of Rb) are taken from [3]. The vapor pressure at 25°C and the vapor pressure curve in Fig. 1 are taken from the vapor-pressure model given by [5], which is

$$\begin{aligned} \log_{10} P_v &= 2.881 + 4.857 - \frac{4215}{T} & (\text{solid phase}) \\ \log_{10} P_v &= 2.881 + 4.312 - \frac{4040}{T} & (\text{liquid phase}), \end{aligned} \tag{1}$$

where P_v is the vapor pressure in torr (for P_v in atmospheres, simply omit the 2.881 term), and T is the temperature in K. This model is specified to have an accuracy better than $\pm 5\%$ from 298–550K. Older, and probably less-accurate, sources of vapor-pressure data include Refs. [6] and [7]. The ionization limit is the minimum energy required to ionize a ^{87}Rb atom; this value is taken from Ref. [8].

The optical properties of the ^{87}Rb D line are given in Tables 3 and 4. The properties are given separately for each of the two D-line components; the D₂ line (the $5^2\text{S}_{1/2} \rightarrow 5^2\text{P}_{3/2}$ transition) properties are given in Table 3, and the optical properties of the D₁ line (the $5^2\text{S}_{1/2} \rightarrow 5^2\text{P}_{1/2}$ transition) are given in Table 4. Of these two components, the D₂ transition is of much more relevance to current quantum and atom optics experiments, because it has a cycling transition that is used for cooling and trapping ^{87}Rb . The frequency ω_0 of the D₂ was measured in [9], while the frequency of the D₁ transition is an average of values given by [10] and [11]; the vacuum wavelengths λ and the wave numbers k_L are then determined via the following relations:

$$\lambda = \frac{2\pi c}{\omega_0} \quad k_L = \frac{2\pi}{\lambda}. \tag{2}$$

Due to the different nuclear masses of the two isotopes ^{85}Rb and ^{87}Rb , the transition frequencies of ^{87}Rb are shifted slightly up compared to those of ^{85}Rb . This difference is reported as the isotope shift, and the values are taken from [10]. (See [11, 12] for less accurate measurements.) The air wavelength $\lambda_{\text{air}} = \lambda/n$ assumes an index of refraction of $n = 1.000\,267\,308(10)$ for the D₂ line and $n = 1.000\,267\,215(10)$ for the D₁ line, corresponding

to typical laboratory conditions (1 atm pressure, 23°C temperature, and 40% relative humidity). The index of refraction is calculated from the 1993 revision [13] of the Edlén formula [14]:

$$n_{\text{air}} = 1 + \left[\left(8\,342.54 + \frac{2\,406\,147}{130 - \kappa^2} + \frac{15\,998}{38.9 - \kappa^2} \right) \left(\frac{P}{96\,095.43} \right) \left(\frac{1 + 10^{-8}(0.601 - 0.009\,72\,T)P}{1 + 0.003\,6610\,T} \right) - f(0.037\,345 - 0.000\,401\,\kappa^2) \right] \times 10^{-8}. \quad (3)$$

Here, P is the air pressure in Pa, T is the temperature in °C, κ is the vacuum wave number $k_L/2\pi$ in μm^{-1} , and f is the partial pressure of water vapor in the air, in Pa (which can be computed from the relative humidity via the Goff-Gratch equation [15]). This formula is appropriate for laboratory conditions and has an estimated (3σ) uncertainty of 3×10^{-8} from 350-650 nm.¹

The lifetimes are weighted averages² from four recent measurements; the first employed beam-gas-laser spectroscopy [19], with lifetimes of 27.70(4) ns for the $5^2P_{1/2}$ state and 26.24(4) ns for the $5^2P_{3/2}$ state, the second used time-correlated single-photon counting [20], with lifetimes of 27.64(4) ns for the $5^2P_{1/2}$ state and 26.20(9) ns for the $5^2P_{3/2}$ state, the third used photoassociation spectroscopy [21] (as quoted by [20]), with a lifetime of 26.23(6) ns for the $5^2P_{3/2}$ state only, and the fourth also used photoassociation spectroscopy [22], with lifetimes of 27.75(8) ns for the $5^2P_{1/2}$ state and 26.25(8) ns for the $5^2P_{3/2}$ state. Note that at present levels of theoretical [23] and experimental accuracy, we do not distinguish between lifetimes of the ^{85}Rb and ^{87}Rb isotopes. Inverting the lifetime gives the spontaneous decay rate Γ (Einstein A coefficient), which is also the natural (homogenous) line width (as an angular frequency) of the emitted radiation.

The spontaneous emission rate is a measure of the relative intensity of a spectral line. Commonly, the relative intensity is reported as an absorption oscillator strength f , which is related to the decay rate by [24]

$$\Gamma = \frac{e^2 \omega_0^2}{2\pi \epsilon_0 m_e c^3} \frac{2J+1}{2J'+1} f \quad (4)$$

for a $J \rightarrow J'$ fine-structure transition, where m_e is the electron mass.

The recoil velocity v_r is the change in the ^{87}Rb atomic velocity when absorbing or emitting a resonant photon, and is given by

$$v_r = \frac{\hbar k_L}{m}. \quad (5)$$

The recoil energy $\hbar\omega_r$ is defined as the kinetic energy of an atom moving with velocity $v = v_r$, which is

$$\hbar\omega_r = \frac{\hbar^2 k_L^2}{2m}. \quad (6)$$

The Doppler shift of an incident light field of frequency ω_L due to motion of the atom is

$$\Delta\omega_d = \frac{v_{\text{atom}}}{c} \omega_L \quad (7)$$

for small atomic velocities relative to c . For an atomic velocity $v_{\text{atom}} = v_r$, the Doppler shift is simply $2\omega_r$. Finally, if one wishes to create a standing wave that is moving with respect to the lab frame, the two traveling-wave components must have a frequency difference determined by the relation

$$v_{\text{sw}} = \frac{\Delta\omega_{\text{sw}}}{2\pi} \frac{\lambda}{2}, \quad (8)$$

¹An uncertainty of 1σ was used in the calculations in this reference, but the real-life uncertainty also has important contributions from the uncertainties of temperature, humidity, and pressure, which are not included here. For more details, see the discussion in Ref. [16].

²Weighted means were computed according to $\mu = (\sum_j x_j w_j) / (\sum_j w_j)$, where the weights w_j were taken to be the inverse variances of each measurement, $w_j = 1/\sigma_j^2$. The variance of the weighted mean was estimated according to $\sigma_\mu^2 = (\sum_j w_j (x_j - \mu)^2) / [(n-1) \sum_j w_j]$, and the uncertainty in the weighted mean is the square root of this variance. See Refs. [17, 18] for more details.

because $\Delta\omega_{\text{sw}}/2\pi$ is the beat frequency of the two waves, and $\lambda/2$ is the spatial periodicity of the standing wave. For a standing wave velocity of v_r , Eq. (8) gives $\Delta\omega_{\text{sw}} = 4\omega_r$. Two temperatures that are useful in cooling and trapping experiments are also given here. The recoil temperature is the temperature corresponding to an ensemble with a one-dimensional rms momentum of one photon recoil $\hbar k_L$:

$$T_r = \frac{\hbar^2 k_L^2}{mk_B}. \quad (9)$$

The Doppler temperature,

$$T_D = \frac{\hbar\Gamma}{2k_B}, \quad (10)$$

is the lowest temperature to which one expects to be able to cool two-level atoms in optical molasses, due to a balance of Doppler cooling and recoil heating [25]. Of course, in Zeeman-degenerate atoms, sub-Doppler cooling mechanisms permit temperatures substantially below this limit [26].

3 Hyperfine Structure

3.1 Energy Level Splittings

The $5^2S_{1/2} \rightarrow 5^2P_{3/2}$ and $5^2S_{1/2} \rightarrow 5^2P_{1/2}$ transitions are the components of a fine-structure doublet, and each of these transitions additionally have hyperfine structure. The fine structure is a result of the coupling between the orbital angular momentum \mathbf{L} of the outer electron and its spin angular momentum \mathbf{S} . The total electron angular momentum is then given by

$$\mathbf{J} = \mathbf{L} + \mathbf{S}, \quad (11)$$

and the corresponding quantum number \mathbf{J} must lie in the range

$$|L - S| \leq J \leq L + S. \quad (12)$$

(Here we use the convention that the magnitude of \mathbf{J} is $\sqrt{J(J+1)}\hbar$, and the eigenvalue of J_z is $m_J\hbar$.) For the ground state in ^{87}Rb , $L = 0$ and $S = 1/2$, so $J = 1/2$; for the first excited state, $L = 1$, so $J = 1/2$ or $J = 3/2$. The energy of any particular level is shifted according to the value of J , so the $L = 0 \rightarrow L = 1$ (D line) transition is split into two components, the D₁ line ($5^2S_{1/2} \rightarrow 5^2P_{1/2}$) and the D₂ line ($5^2S_{1/2} \rightarrow 5^2P_{3/2}$). The meaning of the energy level labels is as follows: the first number is the principal quantum number of the outer electron, the superscript is $2S + 1$, the letter refers to L (i.e., $S \leftrightarrow L = 0$, $P \leftrightarrow L = 1$, etc.), and the subscript gives the value of J .

The hyperfine structure is a result of the coupling of \mathbf{J} with the total nuclear angular momentum \mathbf{I} . The total atomic angular momentum \mathbf{F} is then given by

$$\mathbf{F} = \mathbf{J} + \mathbf{I}. \quad (13)$$

As before, the magnitude of \mathbf{F} can take the values

$$|J - I| \leq F \leq J + I. \quad (14)$$

For the ^{87}Rb ground state, $J = 1/2$ and $I = 3/2$, so $F = 1$ or $F = 2$. For the excited state of the D₂ line ($5^2P_{3/2}$), F can take any of the values 0, 1, 2, or 3, and for the D₁ excited state ($5^2P_{1/2}$), F is either 1 or 2. Again, the atomic energy levels are shifted according to the value of F .

Because the fine structure splitting in ^{87}Rb is large enough to be resolved by many lasers (~ 15 nm), the two D-line components are generally treated separately. The hyperfine splittings, however, are much smaller, and it is useful to have some formalism to describe the energy shifts. The Hamiltonian that describes the hyperfine

structure for each of the D-line components is [24, 27–29]

$$H_{\text{hfs}} = A_{\text{hfs}} \mathbf{I} \cdot \mathbf{J} + B_{\text{hfs}} \frac{3(\mathbf{I} \cdot \mathbf{J})^2 + \frac{3}{2}(\mathbf{I} \cdot \mathbf{J}) - I(I+1)J(J+1)}{2I(2I-1)J(2J-1)} + C_{\text{hfs}} \frac{10(\mathbf{I} \cdot \mathbf{J})^3 + 20(\mathbf{I} \cdot \mathbf{J})^2 + 2(\mathbf{I} \cdot \mathbf{J})[I(I+1) + J(J+1) + 3 - 3I(I+1)J(J+1)] - 5I(I+1)J(J+1)}{I(I-1)(2I-1)J(J-1)(2J-1)}, \quad (15)$$

which leads to a hyperfine energy shift of

$$\Delta E_{\text{hfs}} = \frac{1}{2} A_{\text{hfs}} K + B_{\text{hfs}} \frac{\frac{3}{2} K(K+1) - 2I(I+1)J(J+1)}{4I(2I-1)J(2J-1)} + C_{\text{hfs}} \frac{5K^2(K/4+1) + K[I(I+1) + J(J+1) + 3 - 3I(I+1)J(J+1)] - 5I(I+1)J(J+1)}{I(I-1)(2I-1)J(J-1)(2J-1)}, \quad (16)$$

where

$$K = F(F+1) - I(I+1) - J(J+1), \quad (17)$$

A_{hfs} is the magnetic dipole constant, B_{hfs} is the electric quadrupole constant, and C_{hfs} is the magnetic octupole constant (although the terms with B_{hfs} and C_{hfs} apply only to the excited manifold of the D_2 transition and not to the levels with $J = 1/2$). These constants for the ^{87}Rb D line are listed in Table 5. The value for the ground state A_{hfs} constant is from a recent atomic-fountain measurement [30], while the constants listed for the $5^2P_{3/2}$ manifold were taken from a recent, precise measurement [9]. The A_{hfs} constant for the $5^2P_{1/2}$ manifold is the average from the recent measurements of [10], [11], and [31]; because the discrepancy between the measurements is so large, the older recommended value of [27] is also included in the average (the most recent measurement [31] probably vindicates [10] and rules out [11], but in lieu of a more careful analysis of systematic errors in the experiments, all of the results are simply averaged). These measurements are not yet sufficiently precise to have provided a nonzero value for C_{hfs} , and thus it is not listed. The energy shift given by (16) is relative to the unshifted value (the “center of gravity”) listed in Table 3. The hyperfine structure of ^{87}Rb , along with the energy splitting values, is diagrammed in Figs. 2 and 3.

3.2 Interaction with Static External Fields

3.2.1 Magnetic Fields

Each of the hyperfine (F) energy levels contains $2F+1$ magnetic sublevels that determine the angular distribution of the electron wave function. In the absence of external magnetic fields, these sublevels are degenerate. However, when an external magnetic field is applied, their degeneracy is broken. The Hamiltonian describing the atomic interaction with the magnetic field is

$$\begin{aligned} H_B &= \frac{\mu_B}{\hbar} (g_S \mathbf{S} + g_L \mathbf{L} + g_I \mathbf{I}) \cdot \mathbf{B} \\ &= \frac{\mu_B}{\hbar} (g_S S_z + g_L L_z + g_I I_z) B_z, \end{aligned} \quad (18)$$

if we take the magnetic field to be along the z -direction (i.e., along the atomic quantization axis). In this Hamiltonian, the quantities g_S , g_L , and g_I are respectively the electron spin, electron orbital, and nuclear “ g -factors” that account for various modifications to the corresponding magnetic dipole moments. The values for these factors are listed in Table 6, with the sign convention of [27]. The value for g_S has been measured very precisely, and the value given is the CODATA recommended value. The value for g_L is approximately 1, but to account for the finite nuclear mass, the quoted value is given by

$$g_L = 1 - \frac{m_e}{m_{\text{nuc}}}, \quad (19)$$

which is correct to lowest order in m_e/m_{nuc} , where m_e is the electron mass and m_{nuc} is the nuclear mass [32]. The nuclear factor g_I accounts for the entire complex structure of the nucleus, and so the quoted value is an experimental measurement [27].

If the energy shift due to the magnetic field is small compared to the fine-structure splitting, then J is a good quantum number and the interaction Hamiltonian can be written as

$$H_B = \frac{\mu_B}{\hbar} (g_J J_z + g_I I_z) B_z. \quad (20)$$

Here, the *Landé factor* g_J is given by [32]

$$\begin{aligned} g_J &= g_L \frac{J(J+1) - S(S+1) + L(L+1)}{2J(J+1)} + g_S \frac{J(J+1) + S(S+1) - L(L+1)}{2J(J+1)} \\ &\simeq 1 + \frac{J(J+1) + S(S+1) - L(L+1)}{2J(J+1)}, \end{aligned} \quad (21)$$

where the second, approximate expression comes from taking the approximate values $g_S \simeq 2$ and $g_L \simeq 1$. The expression here does not include corrections due to the complicated multielectron structure of ^{87}Rb [32] and QED effects [33], so the values of g_J given in Table 6 are experimental measurements. The value for g_J for the ground state is taken from the ratio measurement from [34], with the modern CODATA value for the electron g -factor according to [35] (the values for ^{87}Rb and ^{85}Rb are the same to a few ppb [27].) The value for g_J for the $J = 3/2$ excited state is taken from [27], but with the reanalysis as in [35].

If the energy shift due to the magnetic field is small compared to the hyperfine splittings, then similarly F is a good quantum number, so the interaction Hamiltonian becomes [36]

$$H_B = \mu_B g_F \frac{F_z}{\hbar} B_z, \quad (22)$$

where the hyperfine Landé g -factor is given by

$$\begin{aligned} g_F &= g_J \frac{F(F+1) - I(I+1) + J(J+1)}{2F(F+1)} + g_I \frac{F(F+1) + I(I+1) - J(J+1)}{2F(F+1)} \\ &\simeq g_J \frac{F(F+1) - I(I+1) + J(J+1)}{2F(F+1)}. \end{aligned} \quad (23)$$

The second, approximate expression here neglects the nuclear term, which is a correction at the level of 0.1%, since g_I is much smaller than g_J .

For weak magnetic fields, the interaction Hamiltonian H_B perturbs the zero-field eigenstates of H_{hfs} . To lowest order, the levels split linearly according to [24]

$$\Delta E_{|F m_F\rangle} = \mu_B g_F m_F B_z. \quad (24)$$

The approximate g_F factors computed from Eq. (23) and the corresponding splittings between adjacent magnetic sublevels are given in Figs. 2 and 3. The splitting in this regime is called the *Zeeman effect*.

For strong fields where the appropriate interaction is described by Eq. (20), the interaction term dominates the hyperfine energies, so that the hyperfine Hamiltonian perturbs the strong-field eigenstates $|J m_J I m_I\rangle$. The energies are then given to lowest order by [1]

$$\begin{aligned} E_{|J m_J I m_I\rangle} &\approx A_{\text{hfs}} m_I m_J + B_{\text{hfs}} \frac{9(m_I m_J)^2 - 3J(J+1)m_I^2 - 3I(I+1)m_J^2 + I(I+1)J(J+1)}{4J(2J-1)I(2I-1)} \\ &\quad + \mu_B (g_J m_J + g_I m_I) B. \end{aligned} \quad (25)$$

The energy shift in this regime is called the *Paschen-Back effect*.

For intermediate fields, the energy shift is more difficult to calculate, and in general one must numerically diagonalize $H_{\text{hfs}} + H_B$. A notable exception is the *Breit-Rabi formula* [24, 36, 37], which applies to the ground-state manifold of the D transition:

$$E_{|J=1/2\ m_J\ I\ m_I\rangle} = -\frac{\Delta E_{\text{hfs}}}{2(2I+1)} + g_I \mu_B m_B \pm \frac{\Delta E_{\text{hfs}}}{2} \left(1 + \frac{4m_x}{2I+1} + x^2\right)^{1/2}. \quad (26)$$

In this formula, $\Delta E_{\text{hfs}} = A_{\text{hfs}}(I + 1/2)$ is the hyperfine splitting, $m = m_I \pm m_J = m_I \pm 1/2$ [where the \pm sign is taken to be the same as in (26)], and

$$x = \frac{(g_J - g_I)\mu_B B}{\Delta E_{\text{hfs}}}. \quad (27)$$

In order to avoid a sign ambiguity in evaluating (26), the more direct formula

$$E_{|J=1/2\ m_J\ I\ m_I\rangle} = \Delta E_{\text{hfs}} \frac{I}{2I+1} \pm \frac{1}{2}(g_J + 2Ig_I)\mu_B B \quad (28)$$

can be used for the two states $m = \pm(I + 1/2)$. The Breit-Rabi formula is useful in finding the small-field shift of the “clock transition” between the $m_F = 0$ sublevels of the two hyperfine ground states, which has no first-order Zeeman shift. Using $m = m_F$ for small magnetic fields, we obtain

$$\Delta\omega_{\text{clock}} = \frac{(g_J - g_I)^2 \mu_B^2}{2\hbar \Delta E_{\text{hfs}}} B^2 \quad (29)$$

to second order in the field strength.

If the magnetic field is sufficiently strong that the hyperfine Hamiltonian is negligible compared to the interaction Hamiltonian, then the effect is termed the *normal Zeeman effect* for hyperfine structure. For even stronger fields, there are Paschen-Back and normal Zeeman regimes for the fine structure, where states with different J can mix, and the appropriate form of the interaction energy is Eq. (18). Yet stronger fields induce other behaviors, such as the quadratic Zeeman effect [36], which are beyond the scope of the present discussion.

The level structure of ^{87}Rb in the presence of a magnetic field is shown in Figs. 4-6 in the weak-field (Zeeman) regime through the hyperfine Paschen-Back regime.

3.2.2 Electric Fields

An analogous effect, the *dc Stark effect*, occurs in the presence of a static external electric field. The interaction Hamiltonian in this case is [28, 38, 39]

$$H_E = -\frac{1}{2}\alpha_0 E_z^2 - \frac{1}{2}\alpha_2 E_z^2 \frac{3J_z^2 - J(J+1)}{J(2J-1)}, \quad (30)$$

where we have taken the electric field to be along the z -direction, α_0 and α_2 are respectively termed the *scalar* and *tensor polarizabilities*, and the second (α_2) term is nonvanishing only for the $J = 3/2$ level. The first term shifts all the sublevels with a given J together, so that the Stark shift for the $J = 1/2$ states is trivial. The only mechanism for breaking the degeneracy of the hyperfine sublevels in (30) is the J_z contribution in the tensor term. This interaction splits the sublevels such that sublevels with the same value of $|m_F|$ remain degenerate. An expression for the hyperfine Stark shift, assuming a weak enough field that the shift is small compared to the hyperfine splittings, is [28]

$$\Delta E_{|J\ I\ F\ m_F\rangle} = -\frac{1}{2}\alpha_0 E_z^2 - \frac{1}{2}\alpha_2 E_z^2 \frac{[3m_F^2 - F(F+1)][3X(X-1) - 4F(F+1)J(J+1)]}{(2F+3)(2F+2)F(2F-1)J(2J-1)}, \quad (31)$$

where

$$X = F(F+1) + J(J+1) - I(I+1). \quad (32)$$

For stronger fields, when the Stark interaction Hamiltonian dominates the hyperfine splittings, the levels split according to the value of $|m_J|$, leading to an electric-field analog to the Paschen-Back effect for magnetic fields.

The static polarizability is also useful in the context of optical traps that are very far off resonance (i.e., several to many nm away from resonance, where the rotating-wave approximation is invalid), since the optical potential is given in terms of the ground-state polarizability as $V = -1/2\alpha_0 E^2$, where E is the amplitude of the optical field. A slightly more accurate expression for the far-off resonant potential arises by replacing the static polarizability with the frequency-dependent polarizability [40]

$$\alpha_0(\omega) = \frac{\omega_0^2 \alpha_0}{\omega_0^2 - \omega^2}, \quad (33)$$

where ω_0 is the resonant frequency of the lowest-energy transition (i.e., the D₁ resonance); this approximate expression is valid for light tuned far to the red of the D₁ line.

The ^{87}Rb polarizabilities are tabulated in Table 6. Notice that the *differences* in the excited state and ground state scalar polarizabilities are given, rather than the excited state polarizabilities, since these are the quantities that were actually measured experimentally. The polarizabilities given here are in SI units, although they are often given in cgs units (units of cm^3) or atomic units (units of a_0^3 , where the Bohr radius a_0 is given in Table 1). The SI values can be converted to cgs units via $\alpha[\text{cm}^3] = (100 \cdot h/4\pi\epsilon_0)(\alpha/h)[\text{Hz}/(\text{V}/\text{cm})^2] = 5.955\,214\,861\,985\,943 \times 10^{-22} (\alpha/h)[\text{Hz}/(\text{V}/\text{cm})^2]$ (see [40] for discussion of units), and subsequently the conversion to atomic units is straightforward.

The level structure of ^{87}Rb in the presence of an external dc electric field is shown in Fig. 7 in the weak-field regime through the electric hyperfine Paschen-Back regime.

3.3 Reduction of the Dipole Operator

The strength of the interaction between ^{87}Rb and nearly-resonant optical radiation is characterized by the dipole matrix elements. Specifically, $\langle F\ m_F | \mathbf{er} | F'\ m'_F \rangle$ denotes the matrix element that couples the two hyperfine sublevels $|F\ m_F \rangle$ and $|F'\ m'_F \rangle$ (where the primed variables refer to the excited states and the unprimed variables refer to the ground states). To calculate these matrix elements, it is useful to factor out the angular dependence and write the matrix element as a product of a Clebsch-Gordan coefficient and a reduced matrix element, using the Wigner-Eckart theorem [41]:

$$\langle F\ m_F | \mathbf{er}_q | F'\ m'_F \rangle = \langle F || \mathbf{er} || F' \rangle \langle F\ m_F | F'\ m'_F; 1\ q \rangle. \quad (34)$$

Here, q is an index labeling the component of \mathbf{r} in the spherical basis, and the doubled bars indicate that the matrix element is reduced. We can also write (34) in terms of a Wigner 3- j symbol as

$$\langle F\ m_F | \mathbf{er}_q | F'\ m'_F \rangle = \langle F || \mathbf{er} || F' \rangle (-1)^{F'-1+m_F} \sqrt{2F+1} \begin{pmatrix} F' & 1 & F \\ m'_F & q & -m_F \end{pmatrix}. \quad (35)$$

Notice that the 3- j symbol (or, equivalently, the Clebsch-Gordan coefficient) vanishes unless the sublevels satisfy $m_F = m'_F + q$. This reduced matrix element can be further simplified by factoring out the F and F' dependence into a Wigner 6- j symbol, leaving a further reduced matrix element that depends only on the L , S , and J quantum numbers [41]:

$$\begin{aligned} \langle F || \mathbf{er} || F' \rangle &\equiv \langle J\ I\ F || \mathbf{er} || J'\ I'\ F' \rangle \\ &= \langle J || \mathbf{er} || J' \rangle (-1)^{F'+J+1+I} \sqrt{(2F'+1)(2J+1)} \begin{Bmatrix} J & J' & 1 \\ F' & F & I \end{Bmatrix}. \end{aligned} \quad (36)$$

Again, this new matrix element can be further factored into another 6- j symbol and a reduced matrix element involving only the L quantum number:

$$\begin{aligned} \langle J || \mathbf{er} || J' \rangle &\equiv \langle L\ S\ J || \mathbf{er} || L'\ S'\ J' \rangle \\ &= \langle L || \mathbf{er} || L' \rangle (-1)^{J'+L+1+S} \sqrt{(2J'+1)(2L+1)} \begin{Bmatrix} L & L' & 1 \\ J' & J & S \end{Bmatrix}. \end{aligned} \quad (37)$$

The numerical value of the $\langle J = 1/2 \| \mathbf{er} \| J' = 3/2 \rangle$ (D_2) and the $\langle J = 1/2 \| \mathbf{er} \| J' = 1/2 \rangle$ (D_1) matrix elements are given in Table 7. These values were calculated from the lifetime via the expression [42]

$$\frac{1}{\tau} = \frac{\omega_0^3}{3\pi\epsilon_0\hbar c^3} \frac{2J+1}{2J'+1} |\langle J \| \mathbf{er} \| J' \rangle|^2. \quad (38)$$

We take the values of these matrix elements to be real and positive, with the relative sign determined by Eq. (37). Note that all the equations we have presented here assume the normalization convention

$$\sum_{M'} |\langle J M \| \mathbf{er} \| J' M' \rangle|^2 = \sum_{M'q} |\langle J M \| er_q \| J' M' \rangle|^2 = |\langle J \| \mathbf{er} \| J' \rangle|^2. \quad (39)$$

There is, however, another common convention (used in Ref. [43]) that is related to the convention used here by $(J \| \mathbf{er} \| J') = \sqrt{2J+1} \langle J \| \mathbf{er} \| J' \rangle$. Also, we have used the standard phase convention for the Clebsch-Gordan coefficients as given in Ref. [41], where formulae for the computation of the Wigner 3- j (equivalently, Clebsch-Gordan) and 6- j (equivalently, Racah) coefficients may also be found.

The dipole matrix elements for specific $|F m_F\rangle \rightarrow |F' m'_F\rangle$ transitions are listed in Tables 9-20 as multiples of $\langle J \| \mathbf{er} \| J' \rangle$. The tables are separated by the ground-state F number (1 or 2) and the polarization of the transition (where σ^+ -polarized light couples $m_F \rightarrow m'_F = m_F + 1$, π -polarized light couples $m_F \rightarrow m'_F = m_F$, and σ^- -polarized light couples $m_F \rightarrow m'_F = m_F - 1$).

4 Resonance Fluorescence

4.1 Symmetries of the Dipole Operator

Although the hyperfine structure of ^{87}Rb is quite complicated, it is possible to take advantage of some symmetries of the dipole operator in order to obtain relatively simple expressions for the photon scattering rates due to resonance fluorescence. In the spirit of treating the D_1 and D_2 lines separately, we will discuss the symmetries in this section implicitly assuming that the light is interacting with only one of the fine-structure components at a time. First, notice that the matrix elements that couple to any single excited state sublevel $|F' m'_F\rangle$ add up to a factor that is independent of the particular sublevel chosen,

$$\sum_q |\langle F' (m'_F + q) | er_q | F' m'_F \rangle|^2 = \frac{2J+1}{2J'+1} |\langle J \| \mathbf{er} \| J' \rangle|^2, \quad (40)$$

as can be verified from the dipole matrix element tables. The degeneracy-ratio factor of $(2J+1)/(2J'+1)$ (which is 1 for the D_1 line or 1/2 for the D_2 line) is the same factor that appears in Eq. (38), and is a consequence of the normalization convention (39). The interpretation of this symmetry is simply that all the excited state sublevels decay at the same rate Γ , and the decaying population “branches” into various ground state sublevels.

Another symmetry arises from summing the matrix elements from a single ground-state sublevel to the levels in a particular F' energy level:

$$\begin{aligned} S_{FF'} &:= \sum_q (2F'+1)(2J+1) \left\{ \begin{matrix} J & J' & 1 \\ F' & F & I \end{matrix} \right\}^2 |\langle F m_F | F' (m_F - q); 1 q \rangle|^2 \\ &= (2F'+1)(2J+1) \left\{ \begin{matrix} J & J' & 1 \\ F' & F & I \end{matrix} \right\}^2. \end{aligned} \quad (41)$$

This sum $S_{FF'}$ is independent of the particular ground state sublevel chosen, and also obeys the sum rule

$$\sum_{F'} S_{FF'} = 1. \quad (42)$$

The interpretation of this symmetry is that for an *isotropic* pump field (i.e., a pumping field with equal components in all *three* possible polarizations), the coupling to the atom is independent of how the population is distributed among the sublevels. These factors $S_{FF'}$ (which are listed in Table 8) provide a measure of the relative strength of each of the $F \rightarrow F'$ transitions. In the case where the incident light is isotropic and couples two of the F levels, the atom can be treated as a two-level atom, with an effective dipole moment given by

$$|d_{\text{iso,eff}}(F \rightarrow F')|^2 = \frac{1}{3} S_{FF'} |\langle J || e\mathbf{r} || J' \rangle|^2. \quad (43)$$

The factor of $1/3$ in this expression comes from the fact that any given polarization of the field only interacts with one (of three) components of the dipole moment, so that it is appropriate to average over the couplings rather than sum over the couplings as in (41).

When the light is detuned far from the atomic resonance ($\Delta \gg \Gamma$), the light interacts with several hyperfine levels. If the detuning is large compared to the excited-state frequency splittings, then the appropriate dipole strength comes from choosing any ground state sublevel $|F m_F\rangle$ and summing over its couplings to the excited states. In the case of π -polarized light, the sum is independent of the particular sublevel chosen:

$$\sum_{F'} (2F' + 1)(2J + 1) \left\{ \begin{matrix} J & J' & 1 \\ F' & F & I \end{matrix} \right\}^2 |\langle F m_F | F' m_F; 1 0 \rangle|^2 = \frac{1}{3}. \quad (44)$$

This sum leads to an effective dipole moment for far detuned radiation given by

$$|d_{\text{det,eff}}|^2 = \frac{1}{3} |\langle J || e\mathbf{r} || J' \rangle|^2. \quad (45)$$

The interpretation of this factor is also straightforward. Because the radiation is far detuned, it interacts with the full $J \rightarrow J'$ transition; however, because the light is linearly polarized, it interacts with only one component of the dipole operator. Then, because of spherical symmetry, $|\hat{d}|^2 \equiv |e\hat{r}|^2 = e^2(|\hat{x}|^2 + |\hat{y}|^2 + |\hat{z}|^2) = 3e^2|\hat{z}|^2$. Note that this factor of $1/3$ also appears for σ^\pm light, but only when the sublevels are uniformly populated (which, of course, is not the equilibrium configuration for these polarizations). The effective dipole moments for this case and the case of isotropic pumping are given in Table 7.

4.2 Resonance Fluorescence in a Two-Level Atom

In these two cases, where we have an effective dipole moment, the atoms behave like simple two-level atoms. A two-level atom interacting with a monochromatic field is described by the *optical Bloch equations* [42],

$$\begin{aligned} \dot{\rho}_{gg} &= \frac{i\Omega}{2}(\tilde{\rho}_{ge} - \tilde{\rho}_{eg}) + \Gamma\rho_{ee} \\ \dot{\rho}_{ee} &= -\frac{i\Omega}{2}(\tilde{\rho}_{ge} - \tilde{\rho}_{eg}) - \Gamma\rho_{ee} \\ \dot{\tilde{\rho}}_{ge} &= -(\gamma + i\Delta)\tilde{\rho}_{ge} - \frac{i\Omega}{2}(\rho_{ee} - \rho_{gg}), \end{aligned} \quad (46)$$

where the ρ_{ij} are the matrix elements of the density operator $\hat{\rho} := |\psi\rangle\langle\psi|$, $\Omega := -\mathbf{d} \cdot \mathbf{E}_0/\hbar$ is the resonant Rabi frequency, \mathbf{d} is the dipole operator, \mathbf{E}_0 is the electric field amplitude ($\mathbf{E} = \mathbf{E}_0 \cos\omega_L t$), $\Delta := \omega_L - \omega_0$ is the detuning of the laser field from the atomic resonance, $\Gamma = 1/\tau$ is the natural decay rate of the excited state, $\gamma := \Gamma/2 + \gamma_c$ is the “transverse” decay rate (where γ_c is a phenomenological decay rate that models collisions), $\tilde{\rho}_{ge} := \rho_{ge} \exp(-i\Delta t)$ is a “slowly varying coherence,” and $\tilde{\rho}_{ge} = \tilde{\rho}_{eg}^*$. In writing down these equations, we have made the rotating-wave approximation and used a master-equation approach to model spontaneous emission. Additionally, we have ignored any effects due to the motion of the atom and decays or couplings to other auxiliary states. In the case of purely radiative damping ($\gamma = \Gamma/2$), the excited state population settles to the steady state solution

$$\rho_{ee}(t \rightarrow \infty) = \frac{(\Omega/\Gamma)^2}{1 + 4(\Delta/\Gamma)^2 + 2(\Omega/\Gamma)^2}. \quad (47)$$

The (steady state) total photon scattering rate (integrated over all directions and frequencies) is then given by $\Gamma\rho_{ee}(t \rightarrow \infty)$:

$$R_{\text{sc}} = \left(\frac{\Gamma}{2}\right) \frac{(I/I_{\text{sat}})}{1 + 4(\Delta/\Gamma)^2 + (I/I_{\text{sat}})}. \quad (48)$$

In writing down this expression, we have defined the *saturation intensity* I_{sat} such that

$$\frac{I}{I_{\text{sat}}} = 2 \left(\frac{\Omega}{\Gamma}\right)^2, \quad (49)$$

which gives (with $I = (1/2)c\epsilon_0 E_0^2$)

$$I_{\text{sat}} = \frac{c\epsilon_0 \Gamma^2 \hbar^2}{4|\hat{\epsilon} \cdot \mathbf{d}|^2}, \quad (50)$$

where $\hat{\epsilon}$ is the unit polarization vector of the light field, and \mathbf{d} is the atomic dipole moment. With I_{sat} defined in this way, the on-resonance scattering cross section σ , which is proportional to $R_{\text{sc}}(\Delta = 0)/I$, drops to 1/2 of its weakly pumped value σ_0 when $I = I_{\text{sat}}$. More precisely, we can define the scattering cross section σ as the power radiated by the atom divided by the incident energy flux (i.e., so that the scattered power is σI), which from Eq. (48) becomes

$$\sigma = \frac{\sigma_0}{1 + 4(\Delta/\Gamma)^2 + (I/I_{\text{sat}})}, \quad (51)$$

where the on-resonance cross section is defined by

$$\sigma_0 = \frac{\hbar\omega\Gamma}{2I_{\text{sat}}}. \quad (52)$$

Additionally, the saturation intensity (and thus the scattering cross section) depends on the polarization of the pumping light as well as the atomic alignment, although the smallest saturation intensity ($I_{\text{sat}}(m_F = \pm 2 \rightarrow m'_F = \pm 3)$, discussed below) is often quoted as a representative value. Some saturation intensities and scattering cross sections corresponding to the discussions in Section 4.1 are given in Table 7. A more detailed discussion of the resonance fluorescence from a two-level atom, including the spectral distribution of the emitted radiation, can be found in Ref. [42].

4.3 Optical Pumping

If none of the special situations in Section 4.1 applies to the fluorescence problem of interest, then the effects of optical pumping must be accounted for. A discussion of the effects of optical pumping in an atomic vapor on the saturation intensity using a rate-equation approach can be found in Ref. [44]. Here, however, we will carry out an analysis based on the generalization of the optical Bloch equations (46) to the degenerate level structure of alkali

atoms. The appropriate master equation for the density matrix of a $F_g \rightarrow F_e$ hyperfine transition is [1, 45–47]

$$\begin{aligned}
 \frac{\partial}{\partial t} \tilde{\rho}_{\alpha, m_{\alpha}, \beta, m_{\beta}} = & -\frac{i}{2} \left[\delta_{\alpha e} \sum_{m_g} \Omega(m_{\alpha}, m_g) \tilde{\rho}_{g, m_g, \beta, m_{\beta}} - \delta_{g\beta} \sum_{m_e} \Omega(m_e, m_{\beta}) \tilde{\rho}_{\alpha, m_{\alpha}, e, m_e} \right. \\
 & + \delta_{\alpha g} \sum_{m_e} \Omega^*(m_e, m_{\alpha}) \tilde{\rho}_{e, m_e, \beta, m_{\beta}} - \delta_{e\beta} \sum_{m_g} \Omega^*(m_{\beta}, m_g) \tilde{\rho}_{\alpha, m_{\alpha}, g, m_g} \\
 & - \delta_{\alpha e} \delta_{e\beta} \Gamma \tilde{\rho}_{\alpha, m_{\alpha}, \beta, m_{\beta}} \\
 & - \delta_{\alpha e} \delta_{g\beta} \frac{\Gamma}{2} \tilde{\rho}_{\alpha, m_{\alpha}, \beta, m_{\beta}} \\
 & - \delta_{\alpha g} \delta_{e\beta} \frac{\Gamma}{2} \tilde{\rho}_{\alpha, m_{\alpha}, \beta, m_{\beta}} \\
 & + \delta_{\alpha g} \delta_{g\beta} \Gamma \sum_{q=-1}^1 \left[\tilde{\rho}_{e, (m_{\alpha}+q), e, (m_{\beta}+q)} \right. \\
 & \quad \left. \langle F_e, (m_{\alpha}+q) | F_g, m_{\alpha}; 1, q \rangle \langle F_e, (m_{\beta}+q) | F_g, m_{\beta}; 1, q \rangle \right] \\
 & + i(\delta_{\alpha e} \delta_{g\beta} - \delta_{\alpha g} \delta_{e\beta}) \Delta \tilde{\rho}_{\alpha, m_{\alpha}, \beta, m_{\beta}} \Bigg] \left. \begin{array}{l} \text{(pump field)} \\ \text{(dissipation)} \\ \text{(free evolution)} \end{array} \right\} \quad (53)
 \end{aligned}$$

where

$$\begin{aligned}
 \Omega(m_e, m_g) &= \langle F_g, m_g | F_e, m_e; 1, -(m_e - m_g) \rangle \Omega_{-(m_e - m_g)} \\
 &= (-1)^{F_e - F_g + m_e - m_g} \sqrt{\frac{2F_g + 1}{2F_e + 1}} \langle F_e, m_e | F_g, m_g; 1, (m_e - m_g) \rangle \Omega_{-(m_e - m_g)}
 \end{aligned} \quad (54)$$

is the Rabi frequency between two magnetic sublevels,

$$\Omega_q = -\frac{2 \langle F_g || e r || F_e \rangle E_q^{(+)}}{\hbar} \quad (55)$$

is the overall Rabi frequency with polarization q ($E_q^{(+)}$ is the field amplitude associated with the positive-rotating component, with polarization q in the spherical basis), and δ is the Kronecker delta symbol. This master equation ignores coupling to F levels other than the ground (g) and excited (e) levels; hence, this equation is appropriate for a cycling transition such as $F = 2 \rightarrow F' = 3$. Additionally, this master equation assumes purely radiative damping and, as before, does not describe the motion of the atom.

To calculate the scattering rate from a Zeeman-degenerate atom, it is necessary to solve the master equation for the steady-state populations. Then, the total scattering rate is given by

$$R_{\text{sc}} = \Gamma P_e = \Gamma \sum_{m_e} \rho_{e, m_e, e, m_e}, \quad (56)$$

where P_e is the total population in the excited state. In addition, by including the branching ratios of the spontaneous decay, it is possible to account for the polarization of the emitted radiation. Defining the scattering rate $R_{\text{sc}, -q}$ for the polarization $(-q)$, we have

$$R_{\text{sc}, -q} = \sum_{m_e, m_g} |\langle F_e, m_e | F_g, m_g; 1, q \rangle|^2 \rho_{e, m_e, e, m_e}, \quad (57)$$

where, as before, the only nonzero Clebsch-Gordan coefficients occur for $m_e = m_g + q$. As we have defined it here, $q = \pm 1$ corresponds to σ^{\pm} -polarized radiation, and $q = 0$ corresponds to π -polarized radiation. The angular

distribution for the σ^\pm scattered light is simply the classical radiation pattern for a rotating dipole,

$$f_{\text{sc}}^\pm(\theta, \phi) = \frac{3}{16\pi}(1 + \cos^2 \theta), \quad (58)$$

and the angular distribution for the π -scattered light is the classical radiation pattern for an oscillating dipole,

$$f_{\text{sc}}^0(\theta, \phi) = \frac{3}{8\pi} \sin^2 \theta. \quad (59)$$

The net angular pattern will result from the interference of these three distributions.

In general, this master equation is difficult to treat analytically, and even a numerical solution of the time-dependent equations can be time-consuming if a large number of degenerate states are involved. In the following discussions, we will only consider some simple light configurations interacting with the $F = 2 \rightarrow F' = 3$ cycling transition that can be treated analytically. Discussions of Zeeman-degenerate atoms and their spectra can be found in Refs. [47–51].

4.3.1 Circularly (σ^\pm) Polarized Light

The cases where the atom is driven by either σ^+ or σ^- light (i.e. circularly polarized light with the atomic quantization axis aligned with the light propagation direction) are straightforward to analyze. In these cases, the light transfers its angular momentum to the atom, and thus the atomic population is transferred to the state with the largest corresponding angular momentum. In the case of the $F = 2 \rightarrow F' = 3$ cycling transition, a σ^+ driving field will transfer all the atomic population into the $|F = 2, m_F = 2\rangle \rightarrow |F' = 3, m'_F = 3\rangle$ cycling transition, and a σ^- driving field will transfer all the population into the $|F = 2, m_F = -2\rangle \rightarrow |F' = 3, m'_F = -3\rangle$ cycling transition. In both cases, the dipole moment, satisfying

$$|d_{(m_F=\pm 2 \rightarrow m'_F=\pm 3)}|^2 = \frac{2J+1}{2J'+1} |\langle J = 1/2 || e\mathbf{r} || J' = 3/2 \rangle|^2, \quad (60)$$

is given in Table 7. Also, in this case, the saturation intensity reduces to

$$I_{\text{sat}} = \frac{\hbar\omega^3\Gamma}{12\pi c^2}, \quad (61)$$

and the scattering cross section reduces to

$$\sigma_0 = \frac{3\lambda^2}{2\pi}. \quad (62)$$

Note that these values are only valid in steady state. If the pumping field is weak, the “settling time” of the atom to its steady state can be long, resulting in a time-dependent effective dipole moment (and saturation intensity). For example, beginning with a uniform sublevel population in the $F = 2$ ground level, the saturation intensity will begin at 3.5771(10) mW/cm² and equilibrate at 1.669 33(49) mW/cm² for a circularly polarized pump. Also, if there are any “remixing” effects such as collisions or magnetic fields not aligned with the axis of quantization, the system may come to equilibrium in some other configuration.

4.3.2 Linearly (π) Polarized Light

If the light is π -polarized (linearly polarized along the quantization axis), the equilibrium population distribution is more complicated. In this case, the atoms tend to accumulate in the sublevels near $m = 0$. Gao [47] has derived analytic expressions for the equilibrium populations of each sublevel and showed that the equilibrium excited-state population is given by Eq. (47) if Ω^2 is replaced by

$$g_F(2F_g + 1)|\Omega_0|^2, \quad (63)$$

where Ω_0 is the only nonzero component of the Rabi-frequency vector (calculated with respect to the reduced dipole moment $|\langle F || e\mathbf{r} || F' \rangle|^2 = S_{FF'} |\langle J || e\mathbf{r} || J' \rangle|^2$), and g_F is a (constant) geometric factor that accounts for the optical pumping. For the ^{87}Rb $F = 2 \rightarrow F' = 3$ cycling transition, this factor has the value $g_F = 36/461 \approx 0.07809$, leading to a steady-state saturation intensity of $I_{\text{sat}} = 3.053\ 81(89)$ mW/cm².

4.3.3 One-Dimensional $\sigma^+ - \sigma^-$ Optical Molasses

We now consider the important case of an optical molasses in one dimension formed by one σ^+ and one σ^- field (e.g., by two right-circularly polarized, counterpropagating laser fields). These fields interfere to form a field that is linearly polarized, where the polarization vector traces out a helix in space. Because the light is linearly polarized everywhere, and the steady-state populations are independent of the polarization direction (in the plane orthogonal to the axis of quantization), the analysis of the previous section applies. When we apply the formula (48) to calculate the scattering rate, then, we simply use the saturation intensity calculated in the previous section, and use the total intensity (twice the single-beam intensity) for I in the formula. Of course, this steady-state treatment is only strictly valid for a stationary atom, since a moving atom will see a changing polarization and will thus be slightly out of equilibrium, leading to sub-Doppler cooling mechanism [26].

4.3.4 Three-Dimensional Optical Molasses

Finally, we consider an optical molasses in three dimensions, composed of six circularly polarized beams. This optical configuration is found in the commonly used six-beam magneto-optic trap (MOT). However, as we shall see, this optical configuration is quite complicated, and we will only be able to estimate the total rate of fluorescence.

First, we will derive an expression for the electric field and intensity of the light. A typical MOT is formed with two counterpropagating, right-circularly polarized beams along the z -axis and two pairs of counterpropagating, left-circularly polarized beams along the x - and y -axes. Thus, the net electric field is given by

$$\begin{aligned} \mathbf{E}(\mathbf{r}, t) &= \frac{E_0}{2} e^{-i\omega t} \left[e^{ikz} \left(\frac{\hat{x} - i\hat{y}}{\sqrt{2}} \right) + e^{-ikz} \left(\frac{\hat{x} + i\hat{y}}{\sqrt{2}} \right) \right. \\ &\quad \left. + e^{ikx} \left(\frac{\hat{y} + i\hat{z}}{\sqrt{2}} \right) + e^{-ikx} \left(\frac{\hat{y} - i\hat{z}}{\sqrt{2}} \right) + e^{iky} \left(\frac{\hat{z} + i\hat{x}}{\sqrt{2}} \right) + e^{-iky} \left(\frac{\hat{z} - i\hat{x}}{\sqrt{2}} \right) \right] + \text{c.c.} \\ &= \sqrt{2} E_0 \cos \omega t \left[(\cos kz - \sin ky) \hat{x} + (\sin kz + \cos kx) \hat{y} + (\cos ky - \sin kx) \hat{z} \right]. \end{aligned} \quad (64)$$

The polarization is linear everywhere for this choice of phases, but the orientation of the polarization vector is strongly position-dependent. The corresponding intensity is given by

$$I(\mathbf{r}) = I_0 \left[6 - 4(\cos kz \sin ky + \cos ky \sin kx - \sin kz \cos kx) \right], \quad (65)$$

where $I_0 := (1/2)c\epsilon_0 E_0^2$ is the intensity of a single beam. The six beams form an intensity lattice in space, with an average intensity of $6I_0$ and a discrete set of points with zero intensity. Note, however, that the form of this interference pattern is specific to the set of phases chosen here, since there are more than the minimal number of beams needed to determine the lattice pattern.

It is clear that this situation is quite complicated, because an atom moving in this molasses will experience both a changing intensity and polarization direction. The situation becomes even more complicated when the magnetic field gradient from the MOT is taken into account. However, we can estimate the scattering rate if we ignore the magnetic field and assume that the atoms do not remain localized in the lattice, so that they are, on the average, illuminated by all polarizations with intensity $6I_0$. In this case, the scattering rate is given by the two-level atom expression (48), with the saturation intensity corresponding to an isotropic pump field ($I_{\text{sat}} = 3.5771(10) \text{ mW/cm}^2$ for the $F = 2 \rightarrow F' = 3$ cycling transition, ignoring the scattering from any light tuned to the $F = 1 \rightarrow F' = 2$ repump transition). Of course, this is almost certainly an overestimate of the effective saturation intensity, since sub-Doppler cooling mechanisms will lead to optical pumping and localization in the light maxima [52]. These effects can be minimized, for example, by using a very large intensity to operate in the saturated limit, where the scattering rate approaches $\Gamma/2$.

This estimate of the scattering rate is quite useful since it can be used to calculate the number of atoms in an optical molasses from a measurement of the optical scattering rate. For example, if the atoms are imaged by a

CCD camera, then the number of atoms N_{atoms} is given by

$$N_{\text{atoms}} = \frac{8\pi \left[1 + 4(\Delta/\Gamma)^2 + (6I_0/I_{\text{sat}}) \right]}{\Gamma(6I_0/I_{\text{sat}})t_{\text{exp}}\eta_{\text{count}}d\Omega} N_{\text{counts}}, \quad (66)$$

where I_0 is the intensity of one of the six beams, N_{counts} is the integrated number of counts recorded on the CCD chip, t_{exp} is the CCD exposure time, η_{count} is the CCD camera efficiency (in counts/photon), and $d\Omega$ is the solid angle of the light collected by the camera. An expression for the solid angle is

$$d\Omega = \frac{\pi}{4} \left(\frac{f}{(f/\#)d_0} \right)^2, \quad (67)$$

where f is the focal length of the imaging lens, d_0 is the object distance (from the MOT to the lens aperture), and $f/\#$ is the f -number of the imaging system.

5 Data Tables

Table 1: Fundamental Physical Constants (2018 CODATA recommended values [2])

Speed of Light	c	$2.997\,924\,58 \times 10^8$ m/s (exact)
Permeability of Vacuum	μ_0	$4\pi \times 10^{-7}$ N/A ² (exact)
Permittivity of Vacuum	ϵ_0	$(\mu_0 c^2)^{-1}$ (exact) $= 8.854\,187\,817 \dots \times 10^{-12}$ F/m
Planck's Constant	h	$6.626\,070\,15 \times 10^{-34}$ J·s (exact) $4.135\,667\,696 \dots \times 10^{-15}$ eV·s
	\hbar	$1.054\,571\,817 \dots \times 10^{-34}$ J·s $6.582\,119\,569 \dots \times 10^{-16}$ eV·s
Elementary Charge	e	$1.602\,176\,634 \times 10^{-19}$ C (exact)
Bohr Magneton	μ_B	$9.274\,010\,078\,3(28) \times 10^{-24}$ J/T $h \cdot 1.399\,624\,493\,61(42)$ MHz/G
Atomic Mass Unit	u	$1.660\,539\,066\,60(50) \times 10^{-27}$ kg
Electron Mass	m_e	$5.485\,799\,090\,65(16) \times 10^{-4}$ u
		$9.109\,383\,701\,5(28) \times 10^{-31}$ kg
Bohr Radius	a_0	$0.529\,177\,210\,903(80) \times 10^{-10}$ m
Boltzmann's Constant	k_B	$1.380\,649 \times 10^{-23}$ J/K (exact)

Table 2: Rubidium 87 Physical Properties.

Atomic Number	Z	37	
Total Nucleons	$Z + N$	87	
Relative Natural Abundance	$\eta(^{87}\text{Rb})$	27.83(2)%	[3]
Nuclear Lifetime	τ_n	4.88×10^{10} yr	[3]
Atomic Mass	m	86.909 180 520(15) u	[4]
		$1.443\,160\,895\,00(50) \times 10^{-25}$ kg	
Density at 25°C	ρ_m	1.53 g/cm ³	[3]
Melting Point	T_M	39.30 °C	[3]
Boiling Point	T_B	688 °C	[3]
Specific Heat Capacity	c_p	0.363 J/g·K	[3]
Molar Heat Capacity	C_p	31.060 J/mol·K	[3]
Vapor Pressure at 25°C	P_v	$3.92(20) \times 10^{-7}$ torr	[5]
Nuclear Spin	I	3/2	
Ionization Limit	E_I	33 690.804 80(20) cm ⁻¹	[8]
		4.177 127 427(25) eV	

Table 3: Rubidium 87 D₂ ($5^2S_{1/2} \rightarrow 5^2P_{3/2}$) Transition Optical Properties.

Frequency	ω_0	$2\pi \cdot 384.230\,484\,468\,5(62)$ THz	[9]
Transition Energy	$\hbar\omega_0$	1.589 049 602 435(25) eV	
Wavelength (Vacuum)	λ	780.241 209 686(13) nm	
Wavelength (Air)	λ_{air}	780.032 700 9(78) nm	
Wave Number (Vacuum)	$k_L/2\pi$	12 816.549 389 93(21) cm ⁻¹	
Isotope shift	$\omega_0(^{87}\text{Rb}) - \omega_0(^{85}\text{Rb})$	$2\pi \cdot 78.095(12)$ MHz	[10]
Lifetime	τ	26.2348(77) ns	[19–22]
Decay Rate/ Natural Line Width (FWHM)	Γ	$38.117(11) \times 10^6$ s ⁻¹ $2\pi \cdot 6.0666(18)$ MHz	
Absorption oscillator strength	f	0.695 77(20)	
Recoil Velocity	v_r	5.8845 mm/s	
Recoil Energy	ω_r	$2\pi \cdot 3.7710$ kHz	
Recoil Temperature	T_r	361.96 nK	
Doppler Shift ($v_{\text{atom}} = v_r$)	$\Delta\omega_d(v_{\text{atom}} = v_r)$	$2\pi \cdot 7.5419$ kHz	
Doppler Temperature	T_D	145.57 μ K	
Frequency shift for standing wave moving with $v_{\text{sw}} = v_r$	$\Delta\omega_{\text{sw}}(v_{\text{sw}} = v_r)$	$2\pi \cdot 15.0839$ kHz	

Table 4: Rubidium 87 D₁ ($5^2S_{1/2} \rightarrow 5^2P_{1/2}$) Transition Optical Properties.

Frequency	ω_0	$2\pi \cdot 377.107\,463\,380(11)$ THz	[10]
Transition Energy	$\hbar\omega_0$	1.559 591 154 220(46) eV	
Wavelength (Vacuum)	λ	794.978 851 156(23) nm	
Wavelength (Air)	λ_{air}	794.766 477 6(79) nm	
Wave Number (Vacuum)	$k_L/2\pi$	12 578.950 981 47(37) cm ⁻¹	
Isotope shift	$\omega_0(^{87}\text{Rb}) - \omega_0(^{85}\text{Rb})$	$2\pi \cdot 77.583(12)$ MHz	[10]
Lifetime	τ	27.679(27) ns	[19, 20, 22]
Decay Rate/ Natural Line Width (FWHM)	Γ	$36.129(35) \times 10^6$ s ⁻¹ $2\pi \cdot 5.7500(56)$ MHz	
Absorption oscillator strength	f	0.342 31(33)	
Recoil Velocity	v_r	5.7754 mm/s	
Recoil Energy	ω_r	$2\pi \cdot 3.6325$ kHz	
Recoil Temperature	T_r	348.66 nK	
Doppler Shift ($v_{\text{atom}} = v_r$)	$\Delta\omega_d(v_{\text{atom}} = v_r)$	$2\pi \cdot 7.2649$ kHz	
Frequency shift for standing wave moving with $v_{\text{sw}} = v_r$	$\Delta\omega_{\text{sw}}(v_{\text{sw}} = v_r)$	$2\pi \cdot 14.5298$ kHz	

Table 5: Rubidium 87 D Transition Hyperfine Structure Constants.

Magnetic Dipole Constant, $5^2S_{1/2}$	$A_{5^2S_{1/2}}$	$h \cdot 3.417\,341\,305\,452\,145(45)$ GHz	[30]
Magnetic Dipole Constant, $5^2P_{1/2}$	$A_{5^2P_{1/2}}$	$h \cdot 407.25(63)$ MHz	[10, 11, 27]
Magnetic Dipole Constant, $5^2P_{3/2}$	$A_{5^2P_{3/2}}$	$h \cdot 84.7185(20)$ MHz	[9]
Electric Quadrupole Constant, $5^2P_{3/2}$	$B_{5^2P_{3/2}}$	$h \cdot 12.4965(37)$ MHz	[9]

Table 6: Rubidium 87 D Transition Magnetic and Electric Field Interaction Parameters.

Electron spin g -factor	g_s	$2.002\,319\,304\,362\,2(15)$	[53]
Electron orbital g -factor	g_L	$0.999\,993\,69$	
Fine structure Landé g -factor	$g_J(5^2S_{1/2})$	$2.002\,331\,070(26)$	[34, 35]
	$g_J(5^2P_{1/2})$	0.666	
	$g_J(5^2P_{3/2})$	$1.334\,10(20)$	[27, 35]
Nuclear g -factor	g_I	$-0.000\,995\,141\,4(10)$	[27]
Clock transition Zeeman shift	$\Delta\omega_{\text{clock}}/B^2$	$2\pi \cdot 575.15$ Hz/G ²	
Ground-state polarizability	$\alpha_0(5^2S_{1/2})$	$h \cdot 0.0794(16)$ Hz/(V/cm) ²	[40]
D ₁ scalar polarizability	$\alpha_0(5^2P_{1/2}) - \alpha_0(5^2S_{1/2})$	$h \cdot 0.122\,306(16)$ Hz/(V/cm) ²	[54]
D ₂ scalar polarizability	$\alpha_0(5^2P_{3/2}) - \alpha_0(5^2S_{1/2})$	$h \cdot 0.1340(8)$ Hz/(V/cm) ²	[55]
D ₂ tensor polarizability	$\alpha_2(5^2P_{3/2})$	$h \cdot -0.0406(8)$ Hz/(V/cm) ²	[55]

Table 7: Rubidium 87 Dipole Matrix Elements, Saturation Intensities, and Resonant Scattering Cross Sections.

D ₂ (5 ² S _{1/2} → 5 ² P _{3/2}) Transition Dipole Matrix Element	$\langle J = 1/2 er J' = 3/2 \rangle$	4.227 52(62) ea_0 3.584 24(52) $\times 10^{-29}$ C·m
Effective Dipole Moment, Saturation Intensity, and Resonant Cross Section ($F = 2 \rightarrow F' = 3$) (isotropic light polarization)	$d_{\text{iso,eff}}(F = 2 \rightarrow F' = 3)$	2.042 09(30) ea_0 1.731 35(25) $\times 10^{-29}$ C·m
	$I_{\text{sat(iso,eff)}}(F = 2 \rightarrow F' = 3)$	3.5771(10) mW/cm ²
	$\sigma_{0(\text{iso,eff})}(F = 2 \rightarrow F' = 3)$	1.356 456 704 270(44) $\times 10^{-9}$ cm ²
Effective Far-Detuned Dipole Moment, Saturation Intensity, and Resonant Cross Section (D ₂ line, π -polarized light)	$d_{\text{det,eff,D}_2}$	2.440 76(36) ea_0 2.069 36(30) $\times 10^{-29}$ C·m
	$I_{\text{sat(det,eff,D}_2)}$	2.503 99(73) mW/cm ²
	$\sigma_{0(\text{det,eff,D}_2)}$	1.937 795 291 814(62) $\times 10^{-9}$ cm ²
Dipole Moment, Saturation Intensity, and Resonant Cross Section $ F = 2, m_F = \pm 2\rangle \rightarrow F' = 3, m'_F = \pm 3\rangle$ cycling transition (σ^\pm -polarized light)	$d_{(m_F=\pm 2 \rightarrow m'_F=\pm 3)}$	2.989 31(44) ea_0 2.534 44(37) $\times 10^{-29}$ C·m
	$I_{\text{sat}(m_F=\pm 2 \rightarrow m'_F=\pm 3)}$	1.669 33(49) mW/cm ²
	$\sigma_{0(m_F=\pm 2 \rightarrow m'_F=\pm 3)}$	2.906 692 937 721(93) $\times 10^{-9}$ cm ²
D ₁ (5 ² S _{1/2} → 5 ² P _{1/2}) Transition Dipole Matrix Element	$\langle J = 1/2 er J' = 1/2 \rangle$	2.9931(14) ea_0 2.5377(12) $\times 10^{-29}$ C·m
Effective Far-Detuned Dipole Moment, Saturation Intensity, and Resonant Cross Section (D ₁ line, π -polarized light)	$d_{\text{det,eff,D}_1}$	1.728 08(84) ea_0 1.465 13(71) $\times 10^{-29}$ C·m
	$I_{\text{sat(det,eff,D}_1)}$	4.4876(43) mW/cm ²
	$\sigma_{0(\text{det,eff,D}_1)}$	1.005 845 511 294(59) $\times 10^{-9}$ cm ²

Table 8: Rubidium 87 Relative Hyperfine Transition Strength Factors $S_{FF'}$ [from Eq. (41)].

D ₂ (5 ² S _{1/2} → 5 ² P _{3/2}) transition	S_{23}	7/10	S_{12}	5/12
	S_{22}	1/4	S_{11}	5/12
	S_{21}	1/20	S_{10}	1/6
D ₁ (5 ² S _{1/2} → 5 ² P _{1/2}) transition	S_{22}	1/2	S_{12}	5/6
	S_{21}	1/2	S_{11}	1/6

Table 9: Rubidium 87 D₂ ($5^2S_{1/2} \rightarrow 5^2P_{3/2}$) Hyperfine Dipole Matrix Elements for σ^+ transitions ($F = 2, m_F \rightarrow F', m'_F = m_F + 1$), expressed as multiples of $\langle J = 1/2 || er || J' = 3/2 \rangle$.

	$m_F = -2$	$m_F = -1$	$m_F = 0$	$m_F = 1$	$m_F = 2$
$F' = 3$	$\sqrt{\frac{1}{30}}$	$\sqrt{\frac{1}{10}}$	$\sqrt{\frac{1}{5}}$	$\sqrt{\frac{1}{3}}$	$\sqrt{\frac{1}{2}}$
$F' = 2$	$\sqrt{\frac{1}{12}}$	$\sqrt{\frac{1}{8}}$	$\sqrt{\frac{1}{8}}$	$\sqrt{\frac{1}{12}}$	
$F' = 1$	$\sqrt{\frac{1}{20}}$	$\sqrt{\frac{1}{40}}$	$\sqrt{\frac{1}{120}}$		

Table 10: Rubidium 87 D₂ ($5^2S_{1/2} \rightarrow 5^2P_{3/2}$) Dipole Matrix Elements for π transitions ($F = 2, m_F \rightarrow F', m'_F = m_F$), expressed as multiples of $\langle J = 1/2 || er || J' = 3/2 \rangle$.

	$m_F = -2$	$m_F = -1$	$m_F = 0$	$m_F = 1$	$m_F = 2$
$F' = 3$	$-\sqrt{\frac{1}{6}}$	$-\sqrt{\frac{4}{15}}$	$-\sqrt{\frac{3}{10}}$	$-\sqrt{\frac{4}{15}}$	$-\sqrt{\frac{1}{6}}$
$F' = 2$	$-\sqrt{\frac{1}{6}}$	$-\sqrt{\frac{1}{24}}$	0	$\sqrt{\frac{1}{24}}$	$\sqrt{\frac{1}{6}}$
$F' = 1$		$\sqrt{\frac{1}{40}}$	$\sqrt{\frac{1}{30}}$	$\sqrt{\frac{1}{40}}$	

Table 11: Rubidium 87 D₂ ($5^2S_{1/2} \rightarrow 5^2P_{3/2}$) Dipole Matrix Elements for σ^- transitions ($F = 2, m_F \rightarrow F', m'_F = m_F - 1$), expressed as multiples of $\langle J = 1/2 || er || J' = 3/2 \rangle$.

	$m_F = -2$	$m_F = -1$	$m_F = 0$	$m_F = 1$	$m_F = 2$
$F' = 3$	$\sqrt{\frac{1}{2}}$	$\sqrt{\frac{1}{3}}$	$\sqrt{\frac{1}{5}}$	$\sqrt{\frac{1}{10}}$	$\sqrt{\frac{1}{30}}$
$F' = 2$		$-\sqrt{\frac{1}{12}}$	$-\sqrt{\frac{1}{8}}$	$-\sqrt{\frac{1}{8}}$	$-\sqrt{\frac{1}{12}}$
$F' = 1$			$\sqrt{\frac{1}{120}}$	$\sqrt{\frac{1}{40}}$	$\sqrt{\frac{1}{20}}$

Table 12: Rubidium 87 D₂ ($5^2S_{1/2} \rightarrow 5^2P_{3/2}$) Dipole Matrix Elements for σ^+ transitions ($F = 1, m_F \rightarrow F', m'_F = m_F + 1$), expressed as multiples of $\langle J = 1/2 || er || J' = 3/2 \rangle$.

	$m_F = -1$	$m_F = 0$	$m_F = 1$
$F' = 2$	$\sqrt{\frac{1}{24}}$	$\sqrt{\frac{1}{8}}$	$\sqrt{\frac{1}{4}}$
$F' = 1$	$\sqrt{\frac{5}{24}}$	$\sqrt{\frac{5}{24}}$	
$F' = 0$	$\sqrt{\frac{1}{6}}$		

Table 13: Rubidium 87 D₂ ($5^2S_{1/2} \rightarrow 5^2P_{3/2}$) Dipole Matrix Elements for π transitions ($F = 1, m_F \rightarrow F', m'_F = m_F$), expressed as multiples of $\langle J = 1/2 || er || J' = 3/2 \rangle$.

	$m_F = -1$	$m_F = 0$	$m_F = 1$
$F' = 2$	$-\sqrt{\frac{1}{8}}$	$-\sqrt{\frac{1}{6}}$	$-\sqrt{\frac{1}{8}}$
$F' = 1$	$-\sqrt{\frac{5}{24}}$	0	$\sqrt{\frac{5}{24}}$
$F' = 0$		$\sqrt{\frac{1}{6}}$	

Table 14: Rubidium 87 D₂ ($5^2S_{1/2} \rightarrow 5^2P_{3/2}$) Dipole Matrix Elements for σ^- transitions ($F = 1, m_F \rightarrow F', m'_F = m_F - 1$), expressed as multiples of $\langle J = 1/2 || er || J' = 3/2 \rangle$.

	$m_F = -1$	$m_F = 0$	$m_F = 1$
$F' = 2$	$\sqrt{\frac{1}{4}}$	$\sqrt{\frac{1}{8}}$	$\sqrt{\frac{1}{24}}$
$F' = 1$		$-\sqrt{\frac{5}{24}}$	$-\sqrt{\frac{5}{24}}$
$F' = 0$			$\sqrt{\frac{1}{6}}$

Table 15: Rubidium 87 D₁ ($5^2S_{1/2} \rightarrow 5^2P_{1/2}$) Hyperfine Dipole Matrix Elements for σ^+ transitions ($F = 2, m_F \rightarrow F', m'_F = m_F + 1$), expressed as multiples of $\langle J = 1/2 || er || J' = 1/2 \rangle$.

	$m_F = -2$	$m_F = -1$	$m_F = 0$	$m_F = 1$	$m_F = 2$
$F' = 2$	$\sqrt{\frac{1}{6}}$	$\sqrt{\frac{1}{4}}$	$\sqrt{\frac{1}{4}}$	$\sqrt{\frac{1}{6}}$	
$F' = 1$	$\sqrt{\frac{1}{2}}$	$\sqrt{\frac{1}{4}}$	$\sqrt{\frac{1}{12}}$		

Table 16: Rubidium 87 D₁ ($5^2S_{1/2} \rightarrow 5^2P_{1/2}$) Dipole Matrix Elements for π transitions ($F = 2, m_F \rightarrow F', m'_F = m_F$), expressed as multiples of $\langle J = 1/2 || er || J' = 1/2 \rangle$.

	$m_F = -2$	$m_F = -1$	$m_F = 0$	$m_F = 1$	$m_F = 2$
$F' = 2$	$-\sqrt{\frac{1}{3}}$	$-\sqrt{\frac{1}{12}}$	0	$\sqrt{\frac{1}{12}}$	$\sqrt{\frac{1}{3}}$
$F' = 1$		$\sqrt{\frac{1}{4}}$	$\sqrt{\frac{1}{3}}$	$\sqrt{\frac{1}{4}}$	

Table 17: Rubidium 87 D₁ ($5^2S_{1/2} \rightarrow 5^2P_{1/2}$) Dipole Matrix Elements for σ^- transitions ($F = 2, m_F \rightarrow F', m'_F = m_F - 1$), expressed as multiples of $\langle J = 1/2 || er || J' = 1/2 \rangle$.

	$m_F = -2$	$m_F = -1$	$m_F = 0$	$m_F = 1$	$m_F = 2$
$F' = 2$		$-\sqrt{\frac{1}{6}}$	$-\sqrt{\frac{1}{4}}$	$-\sqrt{\frac{1}{4}}$	$-\sqrt{\frac{1}{6}}$
$F' = 1$			$\sqrt{\frac{1}{12}}$	$\sqrt{\frac{1}{4}}$	$\sqrt{\frac{1}{2}}$

Table 18: Rubidium 87 D₁ ($5^2S_{1/2} \rightarrow 5^2P_{1/2}$) Dipole Matrix Elements for σ^+ transitions ($F = 1, m_F \rightarrow F', m'_F = m_F + 1$), expressed as multiples of $\langle J = 1/2 || er || J' = 1/2 \rangle$.

	$m_F = -1$	$m_F = 0$	$m_F = 1$
$F' = 2$	$-\sqrt{\frac{1}{12}}$	$-\sqrt{\frac{1}{4}}$	$-\sqrt{\frac{1}{2}}$
$F' = 1$	$-\sqrt{\frac{1}{12}}$	$-\sqrt{\frac{1}{12}}$	

Table 19: Rubidium 87 D₁ ($5^2S_{1/2} \rightarrow 5^2P_{1/2}$) Dipole Matrix Elements for π transitions ($F = 1, m_F \rightarrow F', m'_F = m_F$), expressed as multiples of $\langle J = 1/2 || er || J' = 1/2 \rangle$.

	$m_F = -1$	$m_F = 0$	$m_F = 1$
$F' = 2$	$\sqrt{\frac{1}{4}}$	$\sqrt{\frac{1}{3}}$	$\sqrt{\frac{1}{4}}$
$F' = 1$	$\sqrt{\frac{1}{12}}$	0	$-\sqrt{\frac{1}{12}}$

Table 20: Rubidium 87 D₁ ($5^2S_{1/2} \rightarrow 5^2P_{1/2}$) Dipole Matrix Elements for σ^- transitions ($F = 1, m_F \rightarrow F', m'_F = m_F - 1$), expressed as multiples of $\langle J = 1/2 || er || J' = 1/2 \rangle$.

	$m_F = -1$	$m_F = 0$	$m_F = 1$
$F' = 2$	$-\sqrt{\frac{1}{2}}$	$-\sqrt{\frac{1}{4}}$	$-\sqrt{\frac{1}{12}}$
$F' = 1$		$\sqrt{\frac{1}{12}}$	$\sqrt{\frac{1}{12}}$

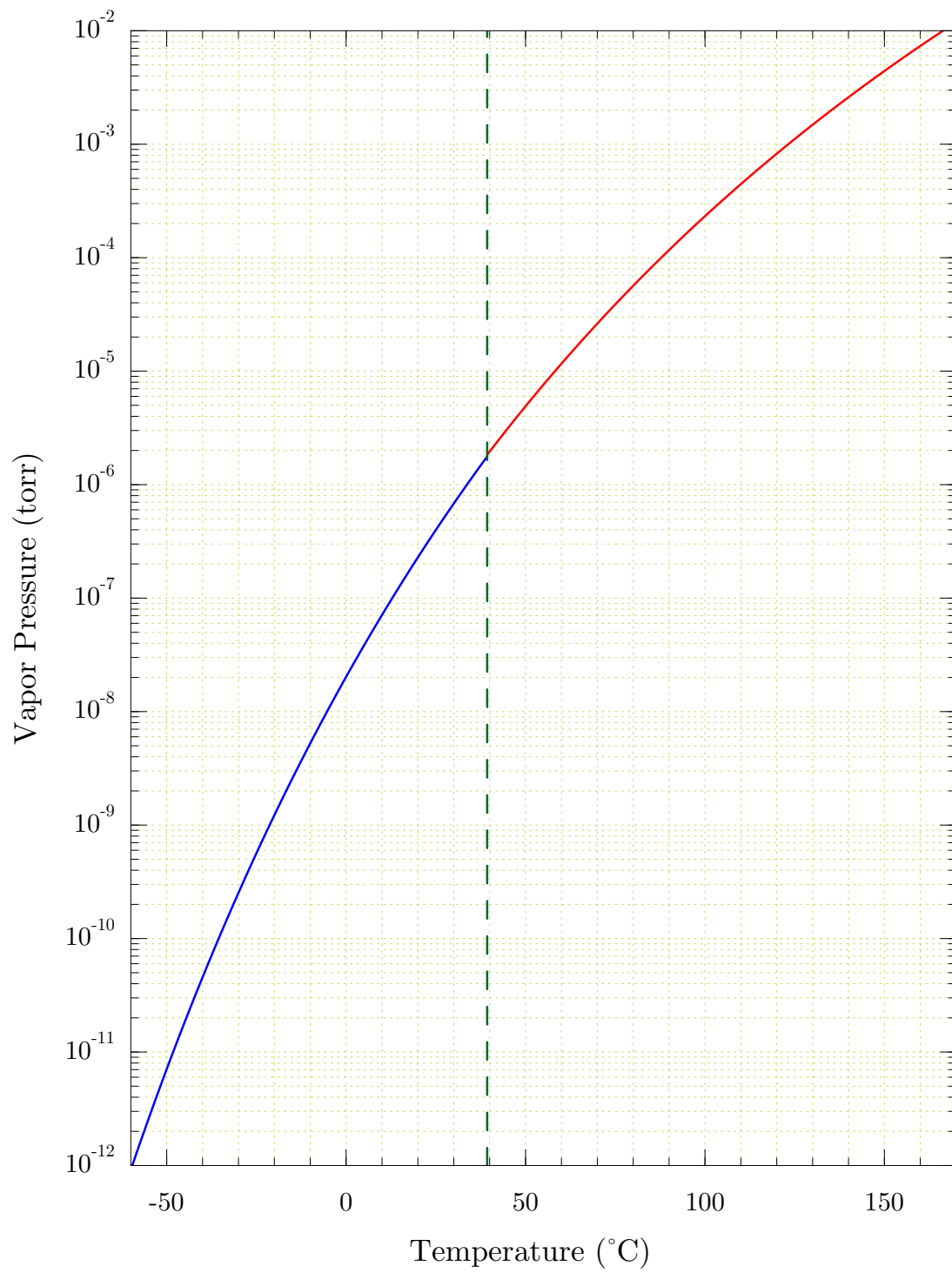


Figure 1: Vapor pressure of rubidium from the model of Eqs. (1). The vertical line indicates the melting point.

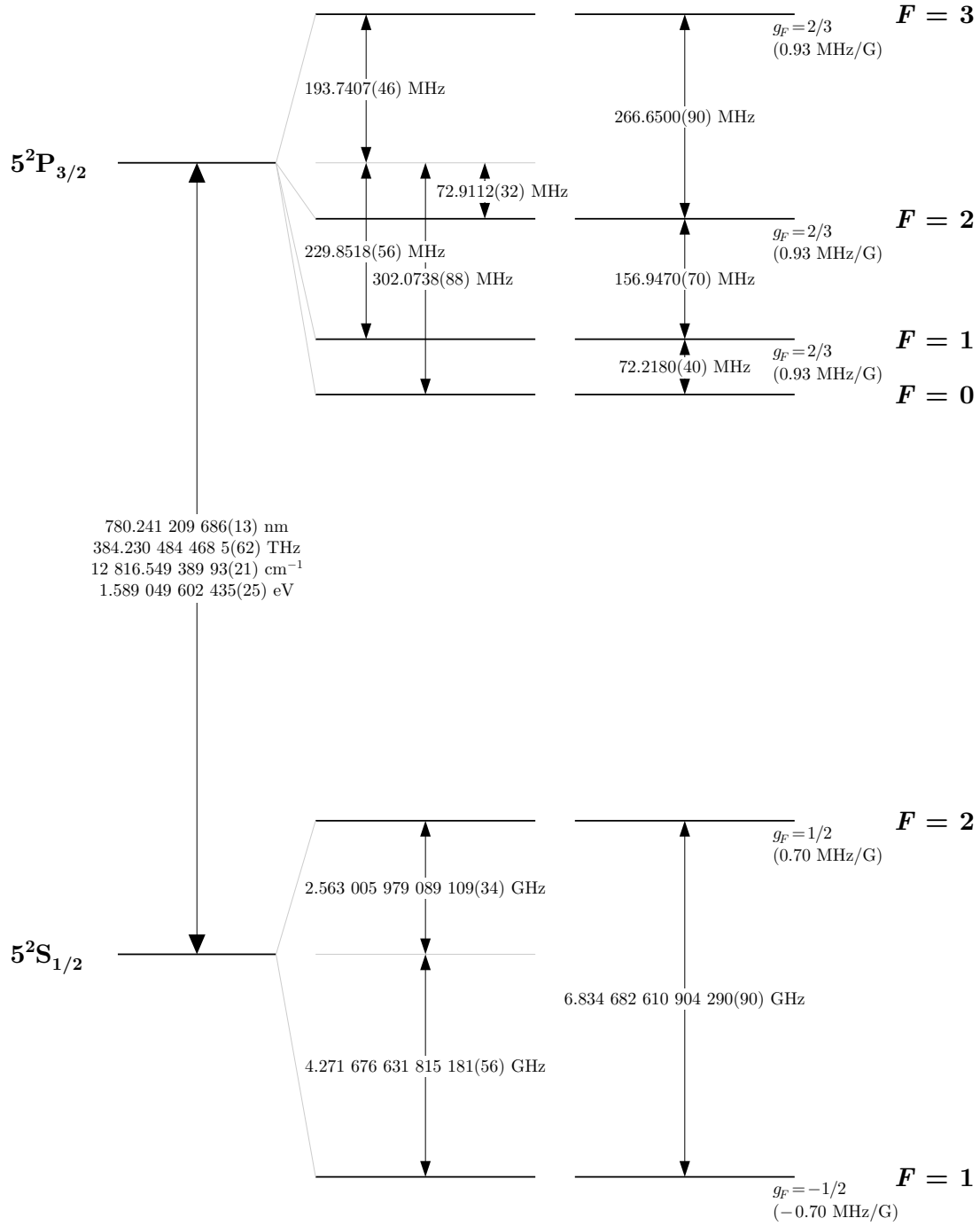


Figure 2: Rubidium 87 D_2 transition hyperfine structure, with frequency splittings between the hyperfine energy levels. The excited-state values are taken from [9], and the ground-state values are from [30]. The relative hyperfine shifts are shown to scale within each hyperfine manifold (but visual spacings should not be compared between manifolds or to the optical splitting). The approximate Landé g_F -factors for each level are also given, with the corresponding Zeeman splittings between adjacent magnetic sublevels.

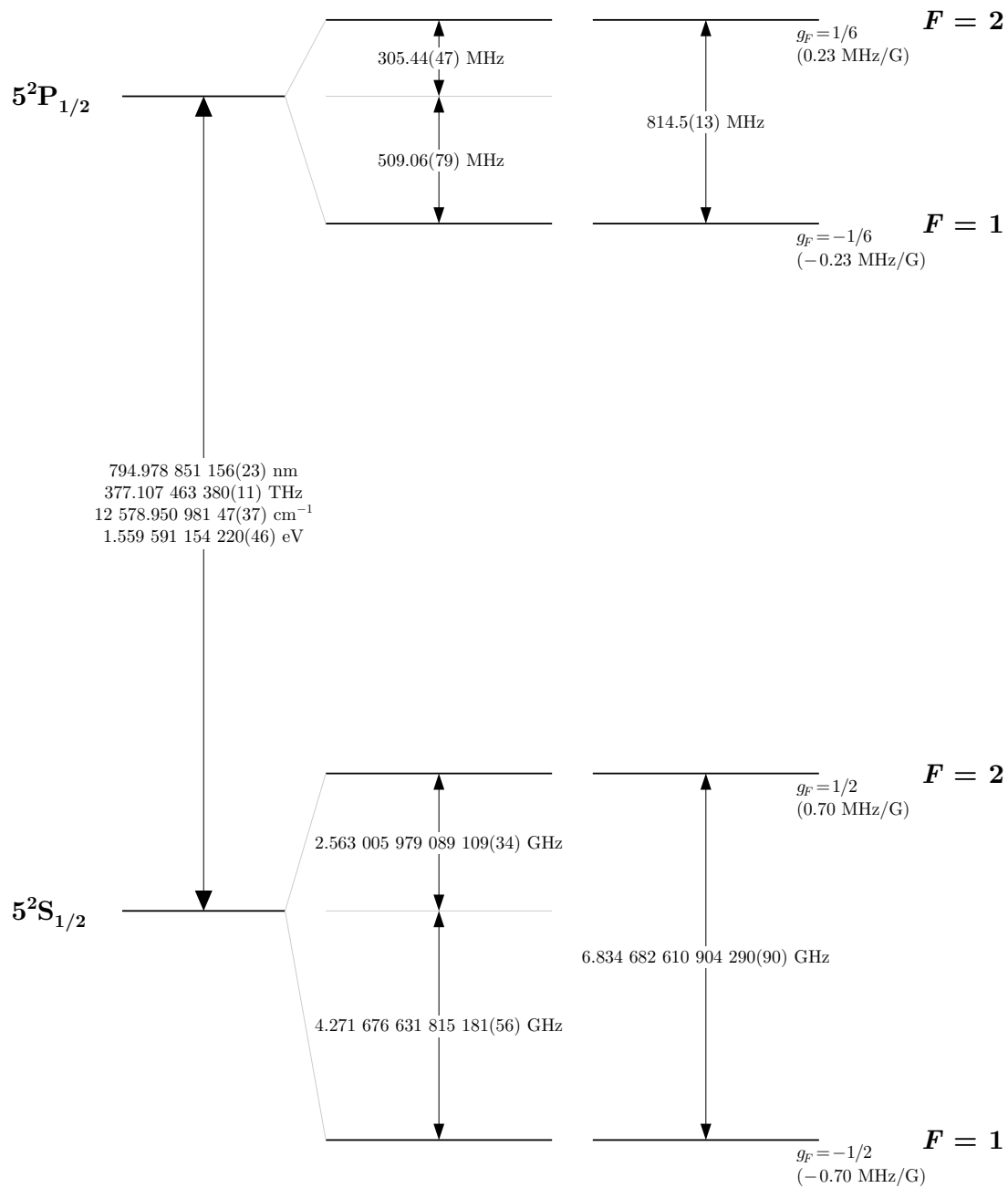


Figure 3: Rubidium 87 D_1 transition hyperfine structure, with frequency splittings between the hyperfine energy levels. The excited-state values are taken from [10, 11, 27], and the ground-state values are from [30]. The relative hyperfine shifts are shown to scale within each hyperfine manifold (but visual spacings should not be compared between manifolds or to the optical splitting). The approximate Landé g_F -factors for each level are also given, with the corresponding Zeeman splittings between adjacent magnetic sublevels.

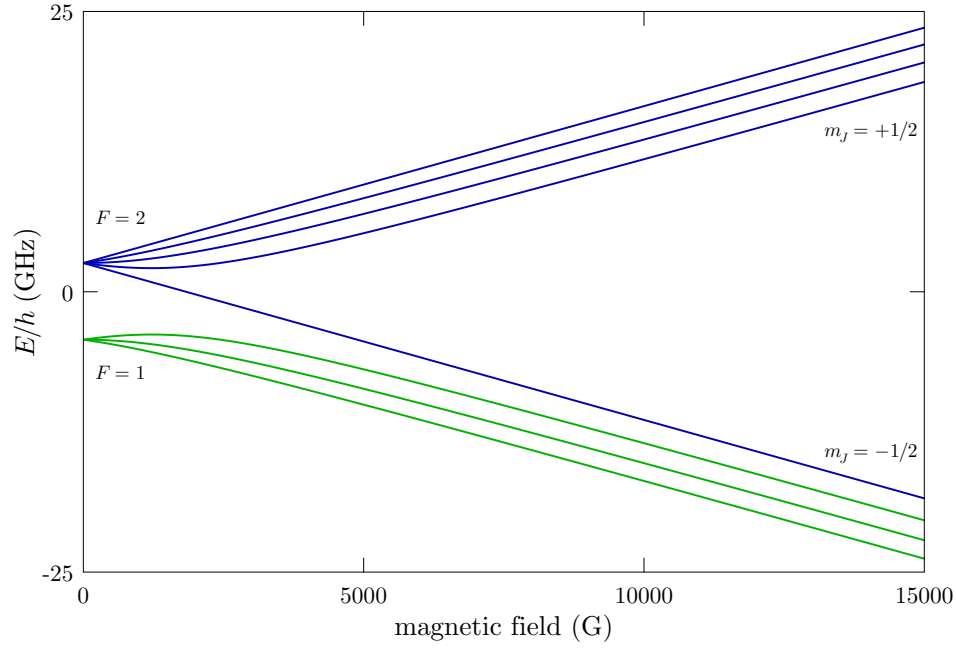


Figure 4: Rubidium 87 $5^2S_{1/2}$ (ground) level hyperfine structure in an external magnetic field. The levels are grouped according to the value of F in the low-field (Zeeman) regime and m_J in the strong-field (hyperfine Paschen-Back) regime.

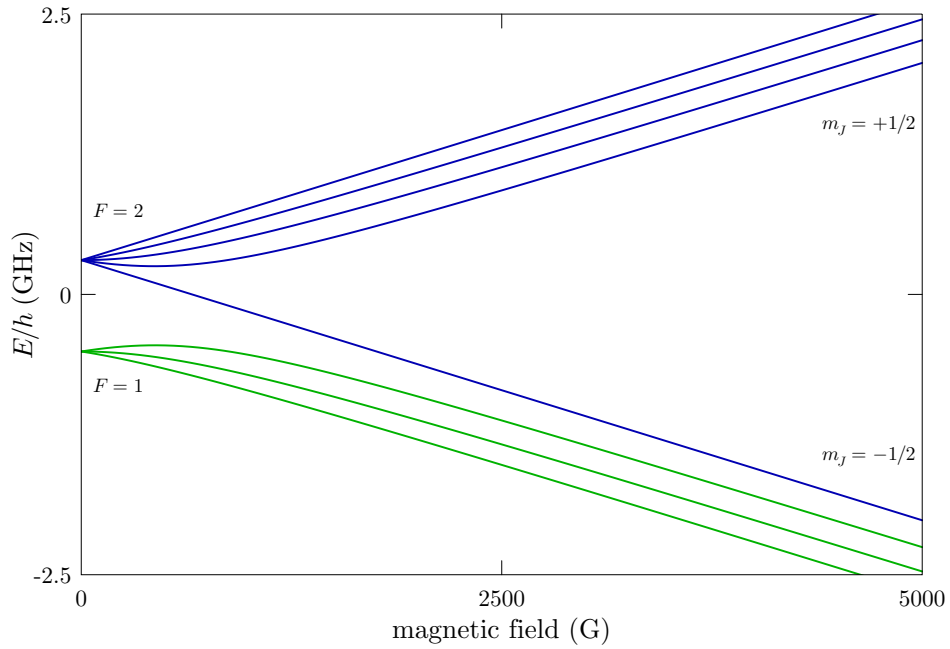


Figure 5: Rubidium 87 $5^2P_{1/2}$ (D_1 excited) level hyperfine structure in an external magnetic field. The levels are grouped according to the value of F in the low-field (Zeeman) regime and m_J in the strong-field (hyperfine Paschen-Back) regime.

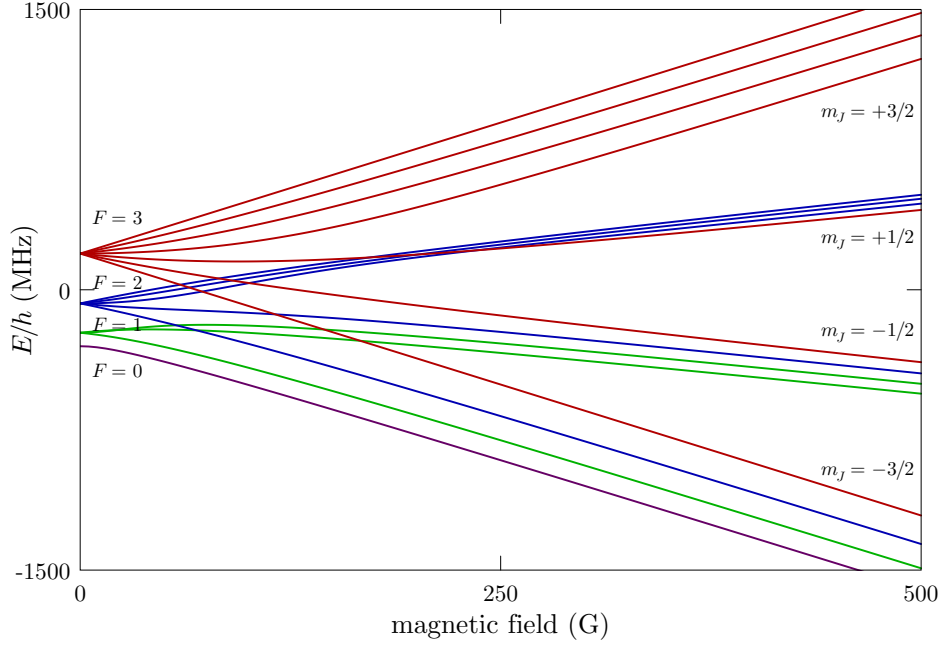


Figure 6: Rubidium 87 $5^2P_{3/2}$ (D_2 excited) level hyperfine structure in an external magnetic field. The levels are grouped according to the value of F in the low-field (Zeeman) regime and m_J in the strong-field (hyperfine Paschen-Back) regime.

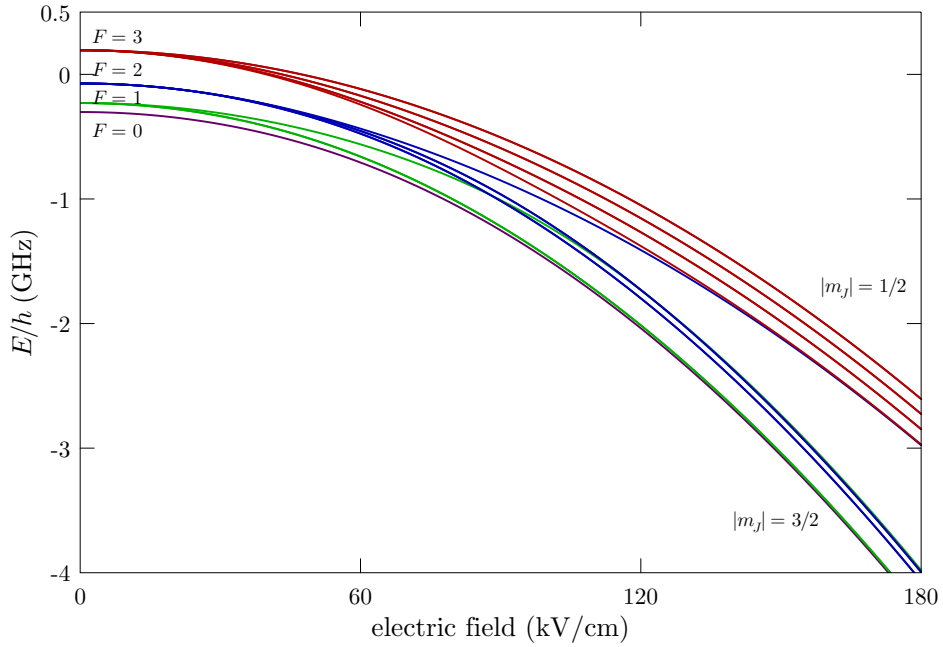


Figure 7: Rubidium 87 $5^2P_{3/2}$ (D_2 excited) level hyperfine structure in a constant, external electric field. The levels are grouped according to the value of F in the low-field (Zeeman) regime and $|m_J|$ in the strong-field (“electric” hyperfine Paschen-Back) regime. Levels with the same values of F and $|m_F|$ (for a weak field) are degenerate.

6 Acknowledgements

Thanks to Windell Oskay, Martin Fischer, Andrew Klekociuk, Mark Saffman, Sadiq Rangwala, Blair Blakie, Markus Kottke, Björn Brezger, Marlon Nakat, Erik Streed, Horst Knöckel, Keith Calkins, Michael Johanning, Greg Smith, Wenhai Ji, Andreas Günther, James Bateman, Brad Foreman, Bruce Klappauf, Ariel Sommer, Alexey Gorshkov, Andrew Jayich, Ara Tonoyan, Zak Vendeiro, Max Mäusezahl, Romain Veyron, Hans Stærkind, Nick Kotsianas, and Jianmin Wang, for corrections and suggestions. Special thanks to Elwin Dijk for a careful review and finding errors in the error propagation.

References

- [1] Daniel A. Steck, “Quantum and Atom Optics,” (2007). Available online at <http://atomoptics.uoregon.edu/~dsteck/teaching/quantum-optics/>.
- [2] Eite Tiesinga, Peter J. Mohr, David B. Newell, and Barry N. Taylor, “CODATA recommended values of the fundamental physical constants: 2018*,” *Reviews of Modern Physics* **93**, 025010 (2021).
- [3] David R. Lide (Ed.), *CRC Handbook of Chemistry and Physics*, 82nd ed. (CRC Press, Boca Raton, 2001).
- [4] Michael P. Bradley, James V. Porto, Simon Rainville, James K. Thompson, and David E. Pritchard, “Penning Trap Measurements of the Masses of ^{133}Cs , $^{87,85}\text{Rb}$, and ^{23}Na with Uncertainties ≤ 0.2 ppb,” *Physical Review Letters* **83**, 4510 (1999).
- [5] C. B. Alcock, V. P. Itkin, and M. K. Horrigan, “Vapor Pressure Equations for the Metallic Elements: 298–2500 K,” *Canadian Metallurgical Quarterly* **23**, 309 (1984).
- [6] A. N. Nesmeyanov, *Vapor Pressure of the Chemical Elements* (Elsevier, Amsterdam, 1963). English edition edited by Robert Gary.
- [7] R. E. Honig, “Vapor Pressure Data for the More Common Elements,” *RCA Review* **18**, 195 (1957).
- [8] S. A. Lee, J. Helmcke, J. L. Hall, and B. P. Stoicheff, “Doppler-free two-photon transitions to Rydberg levels: convenient, useful, and precise reference wavelengths for dye lasers,” *Optics Letters* **3**, 141 (1978).
- [9] Jun Ye, Steve Swartz, Peter Jungner, and John L. Hall, “Hyperfine structure and absolute frequency of the ^{87}Rb $5\text{P}_{3/2}$ state,” *Optics Letters* **21**, 1280 (1996).
- [10] G. P. Barwood, P. Gill, and W. R. C. Rowley, “Frequency Measurements on Optically Narrowed Rb-Stabilised Laser Diodes at 780 nm and 795 nm,” *Applied Physics B* **53**, 142 (1991).
- [11] A. Banerjee, D. Das, and V. Natarajan, “Absolute frequency measurements of the D_1 lines in ^{39}K , ^{85}Rb , and ^{87}Rb with ~ 0.1 ppb uncertainty,” *Europhysics Letters* **65**, 172 (2004).
- [12] Hyatt M. Gibbs and George C. Churchill, “Laser Spectroscopic Measurement of the ^{87}Rb – ^{85}Rb D_1 –Line Isotope Shift,” *Journal of the Optical Society of America* **62**, 1130 (1972).
- [13] K. P. Birch and M. J. Downs, “Letter to the Editor: Correction to the Updated Edlén Equation for the Refractive Index of Air,” *Metrologia* **31**, 315 (1994).
- [14] Bengt Edlén, “The Refractive Index of Air,” *Metrologia* **2**, 12 (1966).
- [15] Holger Vömel, “Saturation vapor pressure formulations,” <http://cires1.colorado.edu/~voemel/vp.html> (2016).
- [16] Jack A. Stone and Jay H. Zimmerman, “Index of Refraction of Air,” <https://emtoolbox.nist.gov/Wavelength/Documentation.asp> (2001).

- [17] E. Richard Cohen and Jesse W. M. DuMond, “Our Knowledge of the Fundamental Constants of Physics of Chemistry in 1965,” *Reviews of Modern Physics* **37**, 537 (1965).
- [18] L. L. Lucas and M. P. Unterwieser, “Comprehensive Review and Critical Evaluation of the Half-Life of Tritium,” *Journal of Research of the National Institute of Standards and Technology* **105**, 541 (2000).
- [19] U. Volz and H. Schmoranzler, “Precision Lifetime Measurements on Alkali Atoms and on Helium by Beam-Gas-Laser Spectroscopy,” *Physica Scripta* **T65**, 48 (1996).
- [20] J. E. Simsarian, L. A. Orozco, G. D. Sprouse, and W. Z. Zhao, “Lifetime measurements of the $7p$ levels of atomic francium,” *Physical Review A* **57**, 2448 (1998).
- [21] H. M. J. M. Boesten, C. C. Tsai, J. R. Gardner, D. J. Heinzen, and B. J. Verhaar, “Observation of a shape resonance in the collision of two cold ^{87}Rb atoms,” *Physical Review A* **55**, 636 (1997).
- [22] R. F. Gutterres, C. Amiot, A. Fioretti, C. Gabbanini, M. Mazzoni, and O. Dulieu, “Determination of the ^{87}Rb $5p$ state dipole matrix element and radiative lifetime from the photoassociation spectroscopy of the Rb_2 $0_g^-(P_{3/2})$ long-range state,” *Physical Review A* **66**, 024502 (2002).
- [23] M. S. Safronova, Carl J. Williams, and Charles W. Clark, “Relativistic many-body calculations of electric-dipole matrix elements, lifetimes, and polarizabilities in rubidium,” *Physical Review A* **69**, 022509 (2004).
- [24] Alan Corney, *Atomic and Laser Spectroscopy* (Oxford, 1977).
- [25] Paul D. Lett, Richard N. Watts, Christoph I. Westbrook, and William D. Phillips, “Observation of Atoms Laser Cooled below the Doppler Limit,” *Physical Review Letters* **61**, 169 (1988).
- [26] J. Dalibard and C. Cohen-Tannoudji, “Laser cooling below the Doppler limit by polarization gradients: simple theoretical models,” *Journal of the Optical Society of America* **6**, 2023 (1989).
- [27] E. Arimondo, M. Inguscio, and P. Violino, “Experimental determinations of the hyperfine structure in the alkali atoms,” *Reviews of Modern Physics* **49**, 31 (1977).
- [28] Lloyd Armstrong, Jr., *Theory of the Hyperfine Structure of Free Atoms* (Wiley-Interscience, New York, 1971).
- [29] Vladislav Gerginov, Andrei Derevianko, and Carol E. Tanner, “Observation of the Nuclear Magnetic Octupole Moment of ^{133}Cs ,” *Physical Review Letters* **91**, 072501 (2003).
- [30] S. Bize, Y. Sortais, M. S. Santos, C. Mandache, A. Clairon, and C. Salomon, “High-accuracy measurement of the ^{87}Rb ground-state hyperfine splitting in an atomic fountain,” *Europhysics Letters* **45**, 558 (1999).
- [31] Andreas Neuzner, Matthias Körber, Stephan Dürr, Gerhard Rempe, and Stephan Ritter, “Breakdown of atomic hyperfine coupling in a deep optical-dipole trap,” *Physical Review A* **92**, 053842 (2015).
- [32] Hans A. Bethe and Edwin E. Salpeter, *Quantum Mechanics of One- and Two-Electron Atoms* (Springer-Verlag, Berlin, 1957).
- [33] Leonti Labzowsky, Igor Goidenko, and Pekka Pyykkö, “Estimates of the bound-state QED contributions to the g -factor of valence ns electrons in alkali metal atoms,” *Physics Letters A* **258**, 31 (1999).
- [34] J. S. Tiedeman and H. G. Robinson, “Determination of $g_J(^1H, ^1S_1/2)/g_S(e)$: Test of Mass-Independent Corrections,” *Physical Review Letters* **39**, 602 (1977).
- [35] D. Ciampini, R. Battesti, C. Rizzo, and E. Arimondo, “Optical spectroscopy of a micro-sized Rb vapor sample in magnetic fields up to 58 T,” *Physical Review A* **96**, 052504 (2017).
- [36] Hans Kleinpoppen, “Atoms,” in Ludwig Bergmann and Clemens Schaefer, *Constituents of Matter: Atoms, Molecules, Nuclei, and Particles*, Wilhelm Raith, Ed. (Walter de Gruyter, Berlin, 1997).

- [37] G. Breit and I. I. Rabi, “Measurement of Nuclear Spin,” *Physical Review* **38**, 2082 (1931).
- [38] Robert W. Schmieder, Allen Lurio, and W. Happer, “Quadratic Stark Effect in the $^2P_{3/2}$ States of the Alkali Atoms,” *Physical Review A* **3**, 1209 (1971).
- [39] Robert W. Schmieder, “Matrix Elements of the Quadratic Stark Effect on Atoms with Hyperfine Structure,” *American Journal of Physics* **40**, 297 (1972).
- [40] Thomas M. Miller, “Atomic and Molecular Polarizabilities,” in *CRC Handbook of Chemistry and Physics*, David R. Lide, Ed., 81st ed. (CRC Press, Boca Raton, 2000).
- [41] D. M. Brink and G. R. Satchler, *Angular Momentum* (Oxford, 1962).
- [42] R. Loudon, *The Quantum Theory of Light*, 2nd ed. (Oxford University Press, 1983).
- [43] Carol E. Tanner, “Precision Measurements of Atomic Lifetimes,” in *Atomic Physics 14: The Fourteenth International Conference on Atomic Physics*, D. J. Wineland, C. E. Wieman, and S. J. Smith, Eds. (AIP Press, 1995).
- [44] J. Sagle, R. K. Namiotka, and J. Huennekens, “Measurement and modelling of intensity dependent absorption and transit relaxation on the cesium D_1 line,” *Journal of Physics B* **29**, 2629 (1996).
- [45] T. A. Brian Kennedy, private communication (1994).
- [46] Claude Cohen-Tannoudji, “Atoms in strong resonant fields,” in *Les Houches, Session XXVII, 1975 — Frontiers in Laser Spectroscopy*, R. Balian, S. Haroche, and S. Liberman, Eds. (North-Holland, Amsterdam, 1977).
- [47] Bo Gao, “Effects of Zeeman degeneracy on the steady-state properties of an atom interacting with a near-resonant laser field: Analytic results,” *Physical Review A* **48**, 2443 (1993).
- [48] Bo Gao, “Effects of Zeeman degeneracy on the steady-state properties of an atom interacting with a near-resonant laser field: Probe spectra,” *Physical Review A* **49**, 3391 (1994).
- [49] Bo Gao, “Effects of Zeeman degeneracy on the steady-state properties of an atom interacting with a near-resonant laser field: Resonance fluorescence,” *Physical Review A* **50**, 4139 (1994).
- [50] D. Polder and M. F. H. Schuurmans, “Resonance fluorescence from a $j = 1/2$ to $j = 1/2$ transition,” *Physical Review A* **14**, 1468 (1976).
- [51] J. Javanainen, “Quasi-Elastic Scattering in Fluorescence from Real Atoms,” *Europhysics Letters* **20**, 395 (1992).
- [52] C. G. Townsend, N. H. Edwards, C. J. Cooper, K. P. Zetie, C. J. Foot, A. M. Steane, P. Szriftgiser, H. Perrin, and J. Dalibard, “Phase-space density in the magneto-optical trap,” *Physical Review A* **52**, 1423 (1995).
- [53] P. J. Mohr, B. N. Taylor, and D. B. Newell, “The 2006 CODATA Recommended Values of the Fundamental Physical Constants, Web Version 5.1,” available at <http://physics.nist.gov/constants> (National Institute of Standards and Technology, Gaithersburg, MD 20899, 31 December 2007).
- [54] K. E. Miller, D. Krause, Jr., and L. R. Hunter, “Precise measurement of the Stark shift of the rubidium and potassium D_1 lines,” *Physical Review A* **49**, 5128 (1994).
- [55] C. Krenn, W. Scherf, O. Khait, M. Musso, and L. Windholz, “Stark effect investigations of resonance lines of neutral potassium, rubidium, europium and gallium,” *Zeitschrift für Physik D* **41**, 229 (1997).